Forschungszentrum Karlsruhe
in der Helmholtz-Gemeinschaft

Wissenschaftliche Berichte
FZKA 6743

INTERNATIONAL FUSION MATERIAL IRRADIATION FACILITY (IFMIF): NEUTRON SOURCE TERM SIMULATION AND NEUTRONICS ANALYSES OF THE HIGH FLUX TEST MODULE

S.P. Simakov, U. Fischer, V. Heinzel, U. von Möllendorff

Institut für Reaktorsicherheit

Forschungszentrum Karlsruhe GmbH, Karlsruhe

2002

Impressum der Print-Ausgabe:

Als Manuskript gedruckt

Forschungszentrum Karlsruhe GmbH
Postfach 3640, 76021 Karlsruhe

Mitglied der Hermann von Helmholtz-Gemeinschaft
Deutscher Forschungszentren (HGF)

ISSN 0947-8620

Abstract

The report describes the new results of the development work performed at Forschungszentrum Karlsruhe on the neutronics of the International Fusion Materials Irradiation Facility (IFMIF). An important step forward has been done in the simulation of neutron production of the deuteron-lithium source using the Li(d,xn) reaction cross sections from evaluated data files. The developed Monte Carlo routine and d-Li reaction data newly evaluated at INPE Obninsk have been verified against available experimental data on the differential neutron yield from deuteron-bombarded thick lithium targets. With the modified neutron source three-dimensional distributions of neutron and photon fluxes, displacement and gas production rates and nuclear heating inside the high flux test module (HFTM) were calculated. In order to estimate the uncertainty resulting from the evaluated data, two independent libraries, recently released by INPE and LANL, have been used in the transport calculations. The proposal to use a reflector around the HFTM to get higher dpa rate and lower spatial gradients was thoroughly investigated. The IFMIF neutronics parameters at different deployment stages regarding variation of beam intensity, footprint and energy have been estimated.

Neutronik des Lithiumtargets und des Hochfluss-Testmoduls der International Fusion Materials Irradiation Facility (IFMIF)

Der Bericht beschreibt neue Ergebnisse der im Forschungszentrum Karlsruhe durchgeführten Entwicklungsarbeiten für die Neutronik der International Fusion Materials Irradiation Facility (IFMIF). Ein wichtiger Schritt vorwärts in der Simulation der Neutronenerzeugung der d-Li-Quelle ist durch die Verwendung von Li(d,xn)-Reaktionsquerschnitten aus ausgewerteten Kerndatensätzen erfolgt. Die dazu entwickelte Monte-Carlo-Routine und bei INPE Obninsk neu ausgewertete d-Li-Reaktionsdaten wurden an vorhandenen experimentellen Daten der differentiellen Neutronenausbeute aus deuteronenbestrahlten dicken Lithiumtargets geprüft. Mit der modifizierten Neutronenquelle wurden dreidimensionale Verteilungen des Neutronen- und Photonenflusses, der Verlagerungs- und Gaserzeugungsraten und der nuklearen Erwärmung im Hochfluss-Testmodul (HFTM) berechnet. Um die von den ausgewerteten Kerndaten stammende Unsicherheit abzuschätzen, wurden in den Transportrechnungen zwei verschiedene kürzlich von INPE und LANL herausgegebene Bibliotheken benutzt. Der Vorschlag, den HFTM mit einem Reflektor zu umgeben, um höhere Verlagerungsraten und kleinere räumliche Gradienten zu erreichen, wurde gründlich untersucht. Die IFMIF-Neutronik-Parameter für verschiedene Ausbaustufen hinsichtlich Strahlintensität, Strahlfleckgröße und Deuteronenenergie wurden abgeschätzt.

Contents

1. Introduction

The International Fusion Materials Irradiation Facility (IFMIF) is an accelerator-based D-Li neutron source with the capability to produce neutrons at sufficient energy, intensity and irradiation volume to test samples of candidate materials up to a full lifetime of anticipated use in fusion energy reactors. IFMIF should be built and operated prior or in parallel to ITER to get experimental data and theoretical knowledge in the field of irradiation effects on fusion materials necessary for DEMO and power fusion reactors projecting [1].

IFMIF is designed under coordination of the International Energy Agency (IAE) by an international team with contributions from the European Union, Japan, Russia and USA. The development of the project has gone through the Conceptual Design Activity and Evaluation in 1995-1998 [2] and is now in the next phase: Key Elements Technology [3]. At this stage, accurate assessment of the d-Li neutron source parameters from basic nuclear processes is required to predict the radiation induced effects in the tested materials during the phase of detailed engineering design, optimisation and cost reduction considerations. In addition to a precise description of the d-Li source term, correct simulation of the neutron transport, displacement damage, gas production and nuclear heating in different materials is necessary.

In earlier work at Forschungszentrum Karlsruhe, computational tools describing neutron production in the deuteron-lithium source were developed and the generation and processing of evaluated nuclear data sets of the major structural materials for neutrons with incident energy up to 50 MeV was started [4, 5]. The approach used for the source neutron simulation was based on simplified, semi-empirical models for the Li(d,xn) reaction cross section. The transport of the neutrons and the nuclear responses were calculated using the first release of the evaluated neutron data library developed in collaboration with INPE Obninsk. Limitations of those approaches and the necessity for the further improvement were expressed by their authors.

Recently evaluated data libraries for complete and detailed description of the deuteron interactions with lithium up to a deuteron energy of 50 MeV have been produced in collaboration with INPE. This opens the opportunity for an advanced modelling of the IFMIF neutron source. Independently, the intense evaluation work performed at Los Alamos National Laboratory (LANL) has resulted in first releases of evaluated neutron transport data libraries for energies up to 150 MeV. This progress has motivated us to implement these achievements in the IFMIF computational analyses by a more advanced modelling the IFMIF neutron source term and performing comprehensive three dimensional neutronics calculations for the high flux test region. Some results were reported elsewhere [6-10].

2. IFMIF reference design and computational model

2.1 IFMIF reference design

This chapter presents an outline of the technical IFMIF features most essential for the present neutronics calculations, namely, the design and specification for the lithium target assembly and the high flux test module (HFTM). These parameters are taken from the reference conceptual design [2].

IFMIF at full performance will employ two continuous-wave linear accelerators each generating 125 mA of 40 MeV deuterons with a beam footprint of 5×20 cm^2 striking a flowing liquid lithium target, Fig. 1. A jet of lithium with 0.512 g/cm^3 density is supposed to be 2.5 cm thick (sufficient to stop 40 MeV deuterons) and 26 cm wide. It is open to the accelerator vacuum and backed by a replaceable backwall 1.8 mm thick, most probably made of steel (Eurofer).

Neutrons produced through the d-Li interaction will irradiate materials located behind the back wall in the beam down-stream direction. In accordance with the level of neutron intensity the space will be subdivided into three regions: High, Medium and Low Flux Test Modules (Fig. 1). The High Flux Test Module (HFTM) placed directly behind the Lithium target is foreseen to be a rectangular volume of 500 cm^3, in which a displacement damage rate of more than 20 dpa (in iron) per full power year will be reachable. The Medium and Low Flux Modules are installed behind the HFTM to utilise the available flux volume for irradiation tests of materials exposed to lower neutron loadings.

The highest irradiation levels in the HFTM correspond to the neutron loading of 1 – 5 MW/cm^2, which materials of the first wall of an ITER or DEMO reactor should withstand. At present, ferritic/martensitic steel (Eurofer), vanadium alloys and possibly silicon carbide ceramics are considered probable candidates. Swelling and creep phenomena, radiation hardening and embrittlement, fracture toughness, crack-growth and many other material properties are the subject of irradiation research. As is well known, the radiation effects strongly depend on the neutron dose, neutron rate, volumetric production of gas atoms like hydrogen or helium, temperature variation and spatial gradients. Thus a special investigation into the nuclear optimization of the HFTM should be undertaken with the main objective to reach the desirable irradiation level and to minimise the spatial gradient of the important nuclear responses such as damage rate. Material conversion caused by the nuclear transmutations should be kept on a negligible level.

In the present reference design the HFTM container houses 27 rigs which hold the material specimens enclosed in capsules. Helium flows through the container and removes the heat induced by neutron reactions, activation and γ-radiation. The resulting power density profiles have to be counterbalanced by electric heaters, so that all specimens can be kept at defined temperatures with rather small spatial gradients. A further heater system has to control the temperature during start-up and shut-down operation of the accelerator.

2.2 Computational model

The computational model used for neutronics analyses should take into account the main and essential features, i.e., geometry configuration and material specifications. The model used in the present analyses is shown in Figs. 2 and 3. Simplifications made with respect to the original design have minor effects and can be taken into account in future analyses. The MCNP code [11, 12], which is the base of our developed computational tools, offers a variety of means for flexible and complete simulation of the real facility.

Each of the two deuteron beams impinges on the target with 10^o declination angle in vertical direction. The beam spatial distribution on the target surface is shown in Fig. 4. It represents the beam profile, which will be formed by the accelerator optical system and delivered to the target. The related simulation routine [5] is rather flexible and is capable to model different

configurations. The profile shown in Fig. 4 is a superposition of a rectangular and several Gaussian distributions, which finally result in a symmetrical Gaussian-edged profile with 20×5 cm^2 beam footprint at half maximum level.

The lithium target and its back plate were simulated as rectangular boxes 26×2.5×20 cm^3 and 26×0.18×20 cm^3 filled with lithium at 0.512 g/cm^3 and Eurofer at 7.8 g/cm^3 density, respectively. Estimations performed have shown that other parts of the lithium jet or back wall, located 5-10 cm above or below the beam foot print, do not affect the irradiation level in the HFTM (i.e., rescattering of source neutrons is negligible).

Since the nuclear and thermal-hydraulic module design is being performed in an iterative process, the starting nuclear calculations therefore assume a simplified HFTM configuration as shown in Fig. 2. The geometrical model consists of a rectangular block 20×5×5 cm^3 filled with Eurofer with a mass density of 6.24 g/cm^3, which is 80% of the normal density to account for the space occupied by cooling gas.

The advanced geometry specification options offered by MCNP4C [12] make it possible to get calculation results in different form for any cell under interest:

(i) averaged over its whole volume,
(ii) 3-d spatial distribution inside and/or outside the cell.

For the latter choice we used a lattice structure for the tallies [12]. For example, for the calculation of the 3-d spatial distribution inside the HFTM, its total volume was divided in 1000 elementary cubic segments 0.5×0.5×0.5 cm^3, for every of which the neutron and photon fluxes, nuclear heating, dpa, helium and hydrogen gas production rate were calculated during one run.

3. d-Li neutron/photon source modelling and verification

3.1 Basic physical processes

The accurate assessment of induced radiation effects in IFMIF test modules will be affected to a large extent by the prediction quality of the spectral and angular distribution of the neutron and photon yields from the d-Li source. To succeed in this the following basic physical processes should be taken into account (Fig. 3):

- the energy, direction and intensity spatial distribution of the incident deuteron beam;
- the slowing down of deuteron in the lithium target;
- deuteron-lithium nuclear interaction resulting to emission of the neutrons and γ-rays.

The profile and parameters of the dual deuteron beams come from the IFMIF design and can be simulated with the necessary accuracy. The deuteron slowing down in the lithium is traditionally accounted for by the theory of ion interaction with atoms. The most crucial and uncertain issue is the modelling of d-Li reaction cross sections. Basically two competing reaction mechanisms should be considered: deuteron stripping and deuteron absorption followed by the formation of a compound nucleus with subsequent particle emission.

Below, three approaches based on different Monte Carlo codes are considered and verified against available experimental data:

M^CDeLi, developed earlier specially for IFMIF neutronics calculations [5];
M^CDeLicious, developed in the present work as a modification of M^CDeLi;

- and the general transport code MCNPX [13], the latest version 2.1.5 of which recently became available.

3.2 Approach based on M^{C}DeLi code

To enable neutronics calculation for IFMIF, the Monte Carlo code M^{C}DeLi was previously developed [5]. It simulates the configuration of dual beams incident on the lithium target surface, the direction of each beam and spatial intensity/current distribution to meet the requirements of the IFMIF project. The process of deuteron slowing down in the lithium medium is treated by the well known empirical model of Ziegler et al. [14].

The neutron production via Li(d,xn) reactions was modelled taking into account two competing reaction mechanisms: deuteron stripping and deuteron absorption by compound nucleus with subsequent emission of one or two neutrons. Free parameters of these models have been adjusted by fits to the angular-energy distributions of the neutron yields from thick lithium targets measured at 32 and 40 MeV incident deuteron energies. The subroutines simulating the deuteron beam configuration, slowing down in the lithium and Li(d,xn) reaction cross sections were linked to the MCNP4B [11] code to enable neutron transport calculations for the IFMIF test modules.

More recently, the M^{C}DeLi code has been intensely tested against available experimental data for the full deuteron range from 5 to 50 MeV [10]. This test has shown that M^{C}DeLi fails to reproduce the data for deuteron energies below 30 MeV (break-down at energies below 15 MeV) and high energy part of neutron spectrum above 40 MeV. In the deuteron energy range 32 – 40 MeV, for which M^{C}DeLi was especially developed, the simplified Li(d,xn) reaction cross sections modelling offers the possibility for further improvement of the quantitative agreement with experimental data.

3.3 Approach based on M^{C}DeLicious code

The drawbacks of M^{C}DeLi approach can be overcome if the simplified semi-empirical model for the Li(d,xn) reaction is replaced by a complete and detailed description of the deuteron interaction with lithium nuclei. This can be accomplished by the use of tabulated data from evaluated data files.

Recently a newly evaluated d-Li data library [15] has been developed in the collaboration of INPE (Obninsk) and FZK (Karlsruhe). Diffraction theory and a modified cascade evaporation model have been applied for calculating the cross sections and angle-energy distributions of reaction products for deuteron energies up to 50 MeV. It turns out that over this energy range, a variety of reaction channels are open for deuterons interacting with lithium nuclei. For example, as Table 1 shows, even for deuteron energies below 6 MeV there are 4 reactions producing neutrons on each isotope. In the INPE evaluation, all channels resulting in the emission of a specific kind of particles are summarized in cumulative particle yields, i.e. there are available in the file production cross sections such as (d,xn), (d,xγ), (d,xα) etc. Several of these cross sections for both of the lithium isotopes are shown in Fig. 5 as a function of the deuteron energy. It is clearly visible that besides elastic deuteron scattering the emission of neutrons, protons, tritium, alpha particles and γ-rays has significant probabilities. For IFMIF neutronics calculations the emission of neutrons and γ-rays is of primary importance since the other particles are short ranged and will be stopped in the lithium target.

Table 1. Reaction channels open in the deuteron–lithium interaction up to 5-6 MeV incident energy, their Q values and thresholds. Neutron producing channels are emphasized by bold font.

d + ^{7}Li			d + ^{6}Li		
Reaction Products	Q, MeV	Threshold, MeV	Reaction Products	Q, MeV	Threshold, MeV
γ + ^{9}Be	16.696	0	2α	22.372	0
n + 2α	**15.122**	**0**	γ + ^{8}Be	22.281	0
n + ^{8}Be	**15.031**	**0**	p + ^{7}Li	5.0254	0
α + ^{5}He	14.232	0	**n + ^{7}Be**	**3.381**	**0**
d + ^{7}Li	0	0	p +t + α	2.558	0
p + ^{8}Li	-0.192	0.247	**n + ^{3}He + α**	**1.795**	**0**
t + ^{6}Li	-0.993	1.278	^{3}He + ^{5}He	0.905	0
n +p + ^{7}Li	**-2.225**	**2.863**	t + ^{5}Li	0.593	0
d +t + α	-2.467	3.175	d + ^{6}Li	0	0
2n + ^{7}Be	**-3.869**	**4.979**	2d + α	-1.474	1.968
^{3}He + ^{6}He	-4.482	5.769	**n +p + ^{6}Li**	**-2.225**	**2.969**
n + p + t + α	**-4.692**	**6.038**	**n + p + d + α**	**-3.699**	**4.937**
…	…	…	…	…	…

To take full advantage of the tabulated d + ^{6,7}Li data, a special routine was developed to read and process the cross sections from the files. As a preliminary step, the ENDF/B-VI formatted data were processed by the NJOY-99 code system [16] into the ACE format suitable for the Monte Carlo sampling scheme. The sampling procedure is as follows. The deuteron track length is sampled, taking into account the total d-Li interaction cross sections read from the file; then for the given deuteron energy the interaction probability with either of the ^{6}Li or ^{7}Li nuclides is calculated according to their macroscopic cross sections; eventually the energy and angle of the generated neutron and photon are sampled. This information together with the coordinates of the d-Li collision inside the lithium target cell is further used for the transport calculations of the neutrons and photons. To enable full neutronics calculations for the IFMIF neutron source, this procedure has been integrated to the M^{C}DeLi code by replacing its d-Li reaction cross section and deuteron slowing down modules. The full package was then compiled with the MCNP4C routines [12], resulting in the advanced M^{C}DeLicious code which is capable of using of evaluated data files for the neutron and photon generation through the d-Li reaction.

The correctness of the NJOY processing and Monte Carlo sampling by the M^{C}DeLicious code was checked by the following procedure. A rather thin target of thickness 0.1 mm filled with the ^{7}Li isotope was considered. The incident deuteron energy was selected in such a way that the energy of the collided deuterons does not deviate very much from an energy point given on the file (e.g., E = 40.00 ± 0.05 MeV). For this energy, the data can be derived from the original INPE file in ENDF format without processing. The neutron and γ-ray yields calculated by M^{C}DeLicious code were converted to double differential cross sections. The comparisons of results for ^{7}Li(d,xn) and ^{7}Li(d,xγ) reactions are shown in Fig. 6 and 7 at 40 MeV deuteron energy. Good agreement is found between the data stored on the original INPE file and those calculated by the M^{C}DeLicious Monte Carlo code using the data processed by NJOY. The remaining inconsistencies are supposed to result from the

differences of the energy and angular bins, interpolation during NJOY-code processing and sampling.

It is worthwhile to note that an evaluation of neutron induced cross sections for the interaction with lithium nuclides was provided by INPE too [15]. Using these evaluated data, it is possible to assess the neutron multiple scattering effect in the lithium target itself as well as the yield of secondary γ-rays due to Li(n,xγ) reactions.

3.4 Approach based on MCNPX code

The Monte Carlo code MCNP4 (versions *a* to *c*) was developed to calculate the transport of neutrons, γ-rays and electrons as a source radiation. The next major extension of this code, MCNPX, enables to track all (including charged) particles up to energies of a few GeV. The presently available version 2.1.5 [13] is not yet capable of using cross sections from evaluated data libraries for charged particles. Instead, it uses various nuclear models, which originally were developed for the intermediate and high energy physics domain. For relatively low incident energies (< 150 MeV) and light target nuclei MCNPX assumes, as default and the best option, the ISABEL intranuclear cascade model. From the methodological point of view MCNPX 2.1.5 resembles the M^{C}DeLi code: both use built-in analytical models for the d + Li interaction. It is questionable, however, if the ISABEL model is able to predict the d-Li neutron source characteristics with sufficient accuracy compared to M^{C}DeLi, which was developed and fitted for this particular reaction and energy range. Nevertheless it is certainly reasonable to start testing MCNPX, since future extensions of the code are announced to be capable of using evaluated charged particle data libraries.

3.5 Comparison with experimental data

There have been a few independent measurements of neutron yield spectra from deuteron bombardment of thick lithium targets [17-25]. The list of experiments in chronological order and the parameters most important for the present analyses are shown in Table 2 (for a comprehensive review of the experiments, their intercomparison and more details see [10] and related original publications).

To simulate these experiments we used a model adapted to a typical experimental configuration: a parallel monoenergetic beam of 1 cm in diameter, a lithium target of 4 cm in diameter and 4 cm thickness, and a neutron detector recording the flux at 500 cm distance from the target. The problem of multiple neutron scattering on the target material (lithium) was investigated by calculations with the newly developed M^{C}DeLicious code and n-Li data from INPE evaluations. In Fig. 8 two neutron spectra are compared: one calculated with the target cell filled by Li at normal density and the other with a void target cell (generation of the source neutrons is the same in both cases). It is seen that the neutron-lithium collisions result in neutron absorption in the target around 20% for neutron energies below 20 MeV and reaching the maximum value of 70% in the vicinity of the 247 keV resonance in the n-Li total cross section. The spectrum averaged correction for neutron absorption in the target material amounts to 10-15% of the neutron flux and should be therefore taken into account when comparing with experimental results.

Fig. 9 compares the experimental total and forward neutron yields with the M^{C}DeLi, M^{C}DeLicious and MCNPX calculations as a function of deuteron energy. Note that the experimental data were measured using different energy thresholds ranging from 0.3 to

3.5 MeV (Table 2). Therefore, the related calculations were performed with a neutron energy threshold of 2 MeV. One can conclude that M^{C}DeLicious with evaluated d-Li data from INPE predicts the energy dependent neutron yield better than M^{C}DeLi or MCNPX do. It is also seen that M^{C}DeLi is not capable of reproducing the experimental data below 20 MeV, whereas MCNPX underestimates the neutron yield by a factor of 2.

Table 2. Parameters of the measurements of neutron spectral and angular distributions from thick Li targets bombarded with deuterons.

No	First Author Year of Publ.	Laboratory, Country	Tar-get	E_d, MeV	Θ, degrees	E_{thr}, MeV	Ref.
1	V.K. Daruga 1968	Inst. of Physics and Power Engi-neering, Russia	Li	22	0^o	1.8	[17]
2	A.N. Weaver 1972	Lawrence Livermore Laboratory, USA	Li	5, 9, 14, 16, 19	3.5^o, 10^o, 18^o, 25^o, 32^o	2.5 1.6	[18]
3	A.N. Goland 1975	Naval Research Laboratory, USA	Li	13.4,19.0, 24.8,28.9, 34.1	0^o, 5^o, 10^o, 15^o, 20^o	3	[19]
4	H.I. Amols 1976	Fermi National Accelerator Laboratory, USA	Li	35	0^o	5	[20]
5	C.E. Nelson 1977	Triangle University Nuclear Laboratory, USA	^{7}Li	8, 12, 15	0^o, 10^o, 20^o, 30^o, 45^o	1	[21]
6	M.A. Lone 1977	Chalk River Nuclear Labo-ratory, Canada	^{7}Li	14.8, 18, 23	0^o, 10^o, 20^o, 30^o, 40^o	0.3	[22]
7	M.J. Saltmarsh 1977	Oak Ridge National Laboratory, USA	Li	40	0^o, 7^o, 15^o, 30^o, 45^o, 60^o, 90^o	2	[23]
8	D.L. Johnson 1979	University of California, USA	Li	35	0^o, 4^o, 8^o, 12^o, 20^o, 30^o, 45^o, 70^o, 105^o, 150^o	1	[24]
9	M. Sugimoto 1995	Japan Energy Research Institute, Japan	Li	32	0^o,5^o,10^o,15^o,20^o, 30^o,40^o,50^o,60^o, 70^o,80^o,90^o,100^o, 110^o,120^o,130^o, 140^o, 150^o	1	[25]

The average energy of neutrons escaping from the thick lithium target in forward direction versus the deuteron energy is depicted in Fig. 10. It is seen that M^{C}DeLi and M^{C}DeLicious exhibit results close to each other and to the experimental data for deuteron energies above 15 MeV, whereas MCNPX overestimates the average neutron energy by 10-50% for all deuteron energies under consideration.

The angular distributions of the emitted neutrons are shown in Fig. 11 for incident deuteron energies 15 to 40 MeV. For deuteron energies 35 and 40 MeV, the three approaches considered in this work give results fluctuating near the experimental data. The MCNPX results, however, reveal a somewhat weaker anisotropy in the forward hemisphere, which is

important for the IFMIF application. With decreasing incident deuteron energy the code outputs deviate more and more from each other and also disagree with the experimental results. At 15-19 MeV deuteron energy, only M^{C}DeLicious provides fairly good agreement with the measured data.

Double differential data – spectral neutron yields at different emission angles – are presented in Fig. 12 and 13 for the two deuteron energies 32 and 40 MeV respectively. These figures again show that M^{C}DeLicious agrees better than M^{C}DeLi and, in particular, MCNPX with the experimental results. It is also revealed that a further essential improvement was achieved with the INPE data in the high energy part of the spectra ($E_n > 30 – 40$ MeV). These neutrons, produced in the exothermic ^{7}Li(d,n)^{8}Be reaction with Q = 15 MeV (Table 1), were not taken into account in the M^{C}DeLi approach. The yield of these high energy neutrons is relatively small (≈ 0.8%), but they will have more significant importance for the activation and shielding behaviour.

The principally new possibility, which the updated code M^{C}DeLicious has opened, is the assessment of the γ-ray yield emitted from the lithium target. There are two physical processes which produce photons in the lithium: first, the primary reaction Li(d,xγ) and, second, neutron induced secondary reactions such as the inelastic scattering of source neutrons on lithium nuclei, i.e., the Li(n,xγ) reaction. Both of these productions paths were analysed by means of M^{C}DeLicious calculations using the evaluated INPE data for d + ^{6,7}Li and n + ^{6,7}Li interactions.

Total and forward (angular distribution is isotropic) photon yields from a thick lithium target bombarded by deuterons, as predicted by M^{C}DeLicious, are shown in Fig. 9 versus the incident deuteron energy. Since experimental data on the Li(d,xγ) reaction are not available, these theoretical predictions cannot be verified at present. The comparison with the neutron yield reveals that the photon yield is one to two orders of magnitude lower. The energy distribution of primary γ-rays, as shown in Fig. 14, consists of two parts: low energy photons ($E_\gamma < 5$ MeV), resulting from Li(d,d'γ), (d,n'γ), (d,p'γ) … reactions; and high energy photons from deuteron capture, i.e., Li(d,γ) reaction. As Fig. 15 shows, the high energy photons amount to 10^{-4} of the total yield and have an average energy ≈ 20 MeV, much larger than the energy (≈ 0.8 MeV) of dominating low energy photons. Although the fraction of high energy photons is relatively small, they will result in activation and transmutation reactions in the IFMIF test modules, since the photo-nuclear reactions have thresholds of a few MeV.

The contribution of the neutron induced γ-ray production depends on the size and mass of the lithium target. For the Li target of the size mentioned above (cylinder ∅4×4 cm, Li-density 0.51 g/cm^3), it amounts to about 8% of the deuteron induced γ-ray yield. The photon energy spectrum, depicted in Fig. 14, reveals that most of the γ-rays have energies below 5 MeV (the discrete lines come from the de-excitation of excited states of the residual nuclei). Nevertheless, also γ-rays with very high energies (10-50 MeV) are produced by neutron capture reactions on target nuclei.

Based on comparisons with available experimental data for deuteron bombarded thick lithium targets, we come to the following conclusions. The updated M^{C}DeLicious code, which is now able to use the INPE evaluation of d-Li cross sections, predicts the neutron source characteristics better than M^{C}DeLi does. M^{C}DeLicious is also able to calculate the photon production in the lithium target, but this could not be verified due to the lack of related

experimental data. The charged particle transport code MCNPX (version 2.1.5) underestimates the neutron yield typically by a factor of 2 and fails to calculate the γ-rays yield.

4. Evaluated nuclear data for neutron and photon transport

4.1. Libraries and processing procedure

Evaluated data for neutron transport calculations have been intensely developed and tested worldwide for many nuclei up to the neutron energy of 20 MeV. As a result such libraries as ENDF, EFF, FENDL, JENDL, BROND and others are now used in many applications. To perform the IFMIF neutronics analyses these libraries need to be extended above 20 MeV, since the d-Li source at 40 MeV deuteron energy produces neutrons with energies up to 55 MeV. Besides the differential cross sections needed for transport calculations the evaluated data libraries should provide as well "engineering" responses, i.e., nuclear heating, gas production and displacement damage rates. At the moment the following data evaluations that meets these requirements are available:

- INPE 50 – developed at the Obninsk Institute of Nuclear Power and Engineering in collaboration with FZK for the nuclides: ^{1}H, ^{6,7}Li, ^{12}C, ^{23}Na, ^{28}Si, ^{39}K, ^{51}V, ^{52}Cr, ^{56}Fe and neutron energies up to 50 MeV [15, 27, 28];
- LANL 150 – developed at Los Alamos National Laboratory for the nuclides: ^{1}H, ^{12}C, ^{16}O, ^{27}Al, ^{28,29,30}Si, ^{31}P, ^{40}Ca, ^{50,52,53,54}Cr, ^{54,56,57,58}Fe, ^{58,60,61,62,64}Ni, ^{63,65}Cu, ^{93}Nb, ^{182,183,184,186}W, ^{206,207,208}Pb and neutron energies up to 150 MeV [29].

To make them available for the Monte Carlo calculations, the original data files in ENDF format must be processed to the ACE format. While the LANL library is already distributed in this format, the processing of the INPE library has been performed by the authors with the NJOY-99 code system [16]. During the processing additional kinds of data were calculated and allocated in the files.

The most important one is the heating due to nuclear reactions, which can be conveniently divided into neutron and photon heating. The neutron heating arises from the kinetic energy of charged products (KERMA factors) and is deposited locally at the point of neutron induced reaction. The HEATR module of NJOY generates heat production cross sections and adds them to the ACE file. The photon heating is proportional to the flux of secondary photons transported from other sites of previous neutron interactions. It is estimated during the coupled neutron-photon transport calculations by MCNP (for this purpose the photon–atom interaction cross section evaluated data from ENDF library [30] are used in the energy range 1 keV – 100 MeV).

The other important design consideration is the damage caused in materials by neutron and photon irradiation. The total energy available to cause displacements is calculated by NJOY from the total kinetic energy of recoil nuclei reduced by the energy lost for electronic excitations (accounted for by the so called Robinson partition function [31]). Eventually, the displacement damage cross sections depends on the damage energy production cross section σ_{Edp} and the energy E_d required to displace an atom from its lattice position:

$$\sigma_{dpa} = 0.8\ \sigma_{Edpa} / 2E_d$$

The values for the effective displacement threshold E_d are chosen to represent experimental results or derived from theoretical calculations. Recommended values can be found in the literature [32]. For some elements, playing key role in the present calculations, the displacement thresholds are presented in Table 3. During the transport calculation the damage rate for the particular material in the selected geometrical cell is computed by folding the estimated spectral neutron flux with the displacement damage cross section.

Table 3. Typical values for the atomic displacement energy E_d needed to compute damage cross sections.

Element	E_d, eV	Element	E_d, eV
Be	31	Co	40
C	31	Ni	40
Mg	25	Cu	40
Al	27	Zr	40
Si	25	Nb	40
Ca	40	Mo	60
Ti	40	Ag	60
V	40	Ta	90
Cr	40	W	90
Mn	40	Au	90
Fe	40	Pb	25

4.2. INPE and LANL libraries intercomparison

As an example of NJOY processed evaluated data, Fig. 16 shows cross-sections from two libraries, LANL and INPE, for one of the most important nuclides, ^{56}Fe. It is seen that these two evaluations reasonably agree with each other, increasing our confidence in the neutronics calculations. The most significant disagreement manifests itself for the neutron energies 20 to 50 MeV, where the neutron yield from Li(d,n) source, as shown in Fig. 16, rapidly decreases. Note also that the INPE evaluated cross sections do not demonstrate resonance behaviour in the energy range 0.2 – 2 MeV, as LANL does. As could be expected, this does not play a significant role in the present calculations because of the relatively small thickness (compare with neutron mean path) of the materials under consideration. Both libraries show that the damage cross sections, gas and heat productions caused by neutrons are increasing function of the energy, underlining the importance of accurate prediction of the high energy part of the source spectrum.

Fig. 17 compares the neutron and photon cross sections and heat deposition in ^{56}Fe. The heating due to photons dominates over neutrons at least by a factor of 10 and is sensitive to both high and low energy photons. On the other hand, the typical photon flux in the HFTM, produced in the lithium target and neutron inelastic collisions, is a few orders of magnitude less than the neutron flux. Thus the final contribution to the total heating will be the balance of these two factors.

The cross sections for some other nuclei, which constitute the materials planned to be irradiated in the IFMIF, are shown in Fig. 18-23. It is interesting to note that the proton production rate exceeds the helium production for every nuclide except carbon, for which the (n,α) reaction is favourable. Such behaviour in the case of carbon obviously is the result of the cluster-like structure of the ^{12}C nucleus and its lower threshold for alpha production (6.2 MeV) as compared to proton production (13.6 MeV). Due to this property a higher rate of

helium production may be expected in carbon containing materials.

For sodium and potassium, which are potential coolant materials for the test module, the evaluated data in the high energy range are incomplete (Fig. 22 and 23). The only available evaluation is that performed at INPE, but it does not contain the total photon, proton and alpha-particle production cross sections. To demonstrate their behaviour up to 20 MeV neutron energy the evaluated cross sections from ENDF/B-VI library are depicted.

Besides neutrons, γ-rays can also produce nuclear transmutations and cause damage in materials due to photo-nuclear reactions. The related cross sections and energy spectra of reaction products were only recently tabulated in specific photo-nuclear evaluated files, e.g., the IAEA or LANL Photonuclear Data Libraries [33, 34], which are complete with respect to radiation transport calculations. Fig. 24 shows some γ-ray induced nuclear reactions cross sections for ^{56}Fe from the IAEA library. Note that photo-nuclear reactions due to their high energy threshold are possible only with hard photons. The fraction of such photons is relatively small. This is why the damage and gas productions due to photons are expected to be negligible. Until now no transport code able to use photonuclear data in a fully-coupled manner is available. Taking this into account we have estimated the contribution of photo-nuclear reactions only for the gas production by folding the γ-ray spectral flux averaged over the cell of interest with the (γ,xp) and (γ,xα) cross sections.

5. Results of neutronics calculations for IFMIF

5.1. Lithium target

Results of neutronics calculations for the lithium target obtained with the M^{C}DeLicious code are listed in Table 4. Given the energy of each beam is 40 MeV and the current – 125 mA, the total power delivered to the lithium jet is 10 MW. This beam will produce 1.1 10^{17} neutrons per second (in 4π solid angle), thus 131 kW will be carried out from the target as neutron kinetic energy. Every 100 deuterons will produce 7.2 neutrons (with mean energy 7.3 MeV) and 1.2 photons (mean energy 0.8 MeV) due to Li(d,xn) and Li(d,xγ) reactions. The number of secondary photons, produced in neutron inelastic collisions with the lithium jet, amounts to 0.1 per 100 deuterons, i.e. one order of magnitude less than the primary γ-ray source.

The deuteron penetration range into the lithium and the energy deposition depend on the rate of energy loss due to deuteron interaction with atoms. For the estimation of the energy loss profile we used the MCNPX code [13], which is able to simulate energy and angle changes resulting from both nuclear and electronic interactions. Given the lithium density of 0.512 g/cm^3, the dependence of the deuteron energy on the penetration depth and the energy deposition profile (at the total beam current of 250 mA) along the beam symmetry line were calculated. The results depicted in Fig. 25 show that the maximum of the beam energy is deposited near the end of the deuteron track, reaching there the extremely high value of more than 300 kW/cm^3. To prevent local lithium boiling, the accelerator beam transport system is planned to introduce an energy dispersion of the incident deuterons. A Gaussian energy distribution with a root mean square (rms) parameter of 0.5 MeV, as shown in Fig. 25, efficiently smears the energy deposition in the vicinity of the peak, resulting in a reduction of the maximum by more than a factor of 2. It is worthwhile to note that the energy dispersion of the incident deuterons slightly increases (by less than 10%) the beam penetration range in the target.

Table 4. Deuteron beam and d-Li source parameters, nuclear induced effects in the lithium target back plate and HFTM.

Parameter	Value	
Li + d Nuclear Radiation Source		
Accelerated Deuteron Energy	40 MeV	
Beam Current	2 beams × 125 mA = 250 mA	
Beam Footprint	20×5 cm^2	
Beam Power	10 MW	
Li Target thickness	2.5 cm	
Li Target density	0.512 g/cm^3	
Mean Deuteron Energy in Li-target	25.4 MeV	
Deuteron Induced Nuclear Reactions	***Li(d,xn)***	***Li(d,xγ)***
Number of *n* or *γ* per 1 *d*	0.072 n/d	0.012 γ/d
Source Intensity (4π)	1.1 10^{17} n/s	1.9 10^{16} γ/s
Source Radiation Power (4π)	131 kW	2.4 kW
Mean *n*- or *γ*- Energy (4π)	7.3 MeV	0.84 MeV
Lithium Target Back Plate (BP)		
Size	$20 \times 5 \times 0.18$ cm^3	
Front Surface	100 cm^2	
Volume	18 cm^3	
Material	Eurofer (Fe-88.9%, Cr–9.6%, C-4.9%,…)	
Material Density	7.8 g/cm^3	
Average Neutron Flux	11.7 10^{14} n/cm^2/s	
Average Neutron Current	7.1 10^{14} n/cm^2/s	
Average Neutron Energy	8.1 MeV	
Neutron and Photon total flux Power	88 + 0.6 kW	
Neutron & Photon Energy Loadings Density	8.8+ 0.06 MW/m^2	
Average Gamma-ray Flux	2.22 10^{14} + 0.95 10^{14} γ/cm^2/s	
Average dpa-rate	54 dpa/fpy	
Average Hydrogen Production	2622 appm/fpy	
Average Helium Production	562 appm/fpy	
Total Heat Production	414 W	
Average Heat Production Density	23 + 2.6 W/cm^3	
High Flux Test Module (HFTM)		
Size	$20 \times 5 \times 5$ cm^3	
Volume	500 cm^3	
Material	Eurofer (Fe-88.9%, Cr–9.6%, C-4.9%,…)	
Material Density	6.24 g/cm^3 (80% of normal)	
Average Neutron Flux	5.86 10^{14} n/cm^2/s	
Average Gamma-ray Flux	2.33 10^{14} + 0.25 10^{14} γ/cm^2/s	
Neutron Energy Load	6.4 (8.3 - 5.0) MW/m^2	
Average dpa-rate	29 dpa/fpy	
Average Hydrogen Production	1577 + 0.008 appm/fpy	
Average Helium Production	340 + 0.0004 appm/fpy	
Total Heat Production	7.0 kW	
Average Heat Production Density	14.0 + 0.5 W/cm^3	

Comments: in right-hand column the first additive in the sum stands for the contribution from the Li(d,xn) reaction, the second – for Li(d,xγ).

5.2. Lithium target back plate

The lithium target back plate obviously must withstand the highest irradiation loadings in the facility. As mentioned above, a stainless steel (Eurofer) is regarded as the most probable material for the target back wall. For the estimation of its replacement period we calculated the main neutronics and irradiation parameters with the M^{C}DeLicious code. Table 4 lists the results averaged over the most strongly irradiated volume $20 \times 5 \times 0.18$ cm^3 of the back plate. It shows that the back wall material should withstand the neutron flux 1.2 10^{15} n/cm^2/s and the energy load density 9 MW/m^2, which is equivalent to 50 dpa per full power year. The neutron irradiation will heat the back wall with 26 W/cm^3 power density.

The spatial distributions of the main nuclear responses are shown in Fig. 26 as contour maps in the X-Y plane. The main topological features reflect the beam density profile in horizontal and vertical directions at the lithium target surface. A relatively large region of moderately flat distribution with highest density of nuclear induced radiation effects is clearly seen in the centre part of the back plate, and regions of high gradients at its edges. The largest gradients of $\approx$ 50%/cm are observed in the horizontal direction at the beam footprint edge near x = 10 cm. This could result in the considerable tensions and degradation of mechanical properties in the back wall material there.

5.3 High Flux Test Module

5.3.1 HFTM volume averaged neutronics parameters

The characteristics of the neutron and photon fluxes, calculated with the M^{C}DeLicious code and averaged over the HFTM volume, are listed in Table 4. The neutron flux, which is the sum of primary and scattered neutrons, has a value of 5.9 10^{14} n/cm^2/s. The γ–ray flux is approximately two times less, 90% of which are photons born in the neutron interaction with the HFTM materials. Table 4 also shows results for radiation induced effects in Eurofer: atom displacement, gas generation and heat production. In particular, it is seen that the assessed averaged displacement rate (29 dpa/fpy) meets the IFMIF reference design requirement to have a 0.5 liter volume with at least 20 dpa/fpy. The average heat deposition in the HFTM is about 14 W/cm^3, comparable with the nuclear heating power density in the first wall of fusion reactors. The total nuclear heating power at the level of 7 kW will require an efficient cooling system for the test module.

The contribution of the photons to the material damage effects was estimated by folding the calculated γ-ray spectra in the HFTM with photo-nuclear reaction cross sections. As Table 4 shows, engineering responses to photons turn out to be less than 5% for the heating and 10^{-3}% for the gas production in comparison with neutrons. Such low sensitivity to photons is due to the softness of the photon spectrum and high thresholds of the relevant reactions (Fig. 24). Regrettably it is impossible to perform a quantitative assessment of the γ–ray contribution to the atom displacement damage, because complete photon-nuclear data libraries are not available.

The neutron energy spectrum averaged over the HFTM is shown in Fig. 27. It is a product of direct d-Li source neutrons and neutrons scattered by the test module, lithium target and back wall. The comparison of M^{C}DeLicious and M^{C}DeLi results reveals some differences in different energy regions, mainly above 40 MeV, where M^{C}DeLicious demonstrates its ability

to predict the neutron yield from the ^{7}Li(d,xn) reaction. The fraction of such neutrons in the total spectrum is 0.8%.

The HFTM/IFMIF neutron spectra are compared as well in Fig. 27 and Table 5 with the spectral fluxes in the first wall of the ITER and DEMO fusion reactors [35]. The latter two have similar shape but different absolute values, reflecting the fact that the first wall of the DEMO (loading of 3.5 MW/m^2) will be exposed to a higher neutron flux than ITER (1.2 MW/m^2). Both spectra contain the well-defined D-T fusion neutron peak, amounting to 21% of the total flux, and a broad spectrum of inelastically scattered and slowed-down neutrons. The mean energy is around 3.5 MeV, whereas there are practically no neutrons exceeding the fusion cut-off energy of 14.6 MeV. In the HFTM of IFMIF an even higher level of the neutron loading (6.4 MW/m^2) will be achieved due to the higher mean energy of neutrons, 7 MeV. The spectral distribution, as Fig. 27 shows, has a broad maximum near 1 MeV and a tail up to 55 MeV. The fraction of neutrons with E > 14.6 MeV amounts to about 50% (Table 5); this constitutes the spectral difference between IFMIF and fusion reactors. These high energy neutrons produce 30 to 80% percent of the displacements and gas atoms. Fortunately, as Table 5 shows, the H/dpa and He/dpa ratios, which affect the radiation behaviour of materials, are comparable with the values calculated for the reactor first wall [35].

Another reason for criticism of IFMIF has been the difference in the cascades produced by primary knock-on atoms with different kinetic energies. Recent theoretical studies [36] based on molecular dynamics simulation have shown that a large cascade of vacancies and interstitials created by a high energy knock-on atom during its evolution rather soon collapses and disintegrates into smaller ones. This means that a difference in the primary knock-on atom energy results in a different number of defects but does not touch the basic mechanisms of radiation damage.

5.3.2 Three-dimensional analyses and HFTM design optimization

The neutronics calculations presented above considered the HFTM as one single cell. Since this cell is located close to the neutron source, the neutron flux and induced nuclear effects will strongly depend on the position inside the test module. On the other hand they will be affected by neutrons scattered on materials which inevitably will surround the test module or could be specially allocated around it to improve some neutronics features, e.g., to minimize spatial gradients, optimise the HFTM geometrical configuration etc. Such analysis can be accomplished by calculating three dimensional distributions inside and outside the HFTM (the method used was described in section 2.2).

The spatial distributions are presented in Figs. 26 to 33 along the depth into HFTM (Z-axis or deuteron beam direction as shown in Fig. 2) starting from selected points at the front plane: geometrical centre of the HFTM, top side centre, corner and right side center. Calculations have been performed with two libraries (LANL and INPE) to test the sensitivity of the results to the evaluated data. The comparison has shown that the neutron and γ-ray fluxes and the dpa-rate agree with each other within 10%. Larger discrepancies, 10 to 20%, are found for the heating, hydrogen and helium production rates. Obviously this is the result of the differences in the KERMA factor, (n,xp) and (n,xα) reaction cross sections as seen in Fig. 16.

Table 5. HFTM/IFMIF neutron flux parameters and radiation induced effects in different materials, comparison with irradiation in the first wall of ITER and DEMO.

Facility	**IFMIF/HFTM**				**ITER**	**DEMO**
Material Parameter	Steel Eurofer	Steel F82H-mod	Vanadium V4Ti4Cr	Ceramic SiC	Iron Fe	Iron Fe
Wall Load, MW/m^2 (Total) (E > 14.6 MeV)	6.4 3.0 (47 %)				1.2 -	3.5 -
n-flux, 10^{14}/cm^2/s (Total) (E > 14.6 MeV)	5.7 1.1 (19%)				4.0 -	13.0
Mean Neutron Energy, MeV (E > 14.6 MeV)	7.0 21				3.6 -	3.2
dpa, 1/fpy (Total) (E > 14.6 MeV)	28 10 (37%)	26 10 (40%)	28 9.9 (35%)	37 5.4 (23%)	12 -	30 -
Volume (dpa > 20/fpy), cm^3	360	330	360	330		
H-production, appm/fpy (Total) (E > 14.6 MeV)	1510 1060(70%)	1150 950(83%)	660 520 (79%)	1260 760 (60%)	540 -	1240 -
Ratio H/dpa (Total) (E > 14.6 MeV)	54 102	44 91	23 53	21 140	45 -	41 -
He-production, appm/fpy (Total) (E > 14.6 MeV)	330 210 (63%)	430 290 (67%)	120 96 (81%)	2590 1770(68%)	140 -	320 -
Ratio He/dpa (Total) (E > 14.6 MeV)	12 20	16 30	4 10	70 320	11 -	10 -
Nuclear Heating, W/cm^3 (Total) (E > 14.6 MeV)	14 6.2 (44%)				12 -	35 -

As one can see, the dpa-rate and gas production are monotonically and rapidly decreasing functions of the depth. This is explained by the dependence of these parameters on the neutron flux, which rapidly decreases with increasing distance from the neutron source. In contrast, the heat production in the HFTM has a lower gradient and is even flat in the front layer of ≈2 cm. The reason is the dominating contribution of photons to the nuclear heating, the spatial distribution of which has a broad maximum along the beam direction. Fig. 34 shows that the photon flux, though it is 2-3 times less than the neutron flux, heats the Eurofer with 2-3 times as much power. This reflects the capability of photons to release much more heating energy in matter than neutrons with the same energy will release (Fig. 17): one order of magnitude for energies above 1 MeV and up to five orders at lower energies.

5.3.3 Reflector effects on the dpa rate and gradient

To attain a higher average displacement rate and flatter spatial distribution in the high flux module, it was proposed to use a reflector around it, that will return some fraction of neutrons back into the HFTM [6]. For quantitative assessment of the reflector effect we used the computational model shown in Figs. 2 and 3. The HFTM was surrounded from all sides (except the side towards the lithium target, the effect of which was found to be negligible) by plates filled with the material at 60-90% of normal density to take into account the heat removing channels.

The following elements were considered as candidates for the reflector: aluminium, carbon, lead, nickel, iron (Eurofer), beryllium and tungsten. The radiation induced effects inside the HFTM were assessed for different reflector thickness. It was found that they increase as the reflector becomes thicker, but reach saturation at 10 cm. For this thickness the most prominent reflecting effect was demonstrated by Eurofer, tungsten and beryllium. Figs. 35 and 36 show calculation results for dpa and heating rates for the bare and surrounded test module along two lines: the HFTM symmetry axis (center) and its corner, where the reflector effects are expected to be strongest. It is clearly visible that the relative increase of displacement damage and heat power density on the periphery amounts to 20-50%, that is, 2 times more than in the central region of the HFTM, 10-20%. This means that reflector indeed results in improved irradiation conditions in the HFTM: the dpa rate increases, and the spatial gradient decreases.

As for the selection of the more optimum material for the reflector, one can see that Be, W and Eurofer equally affect the displacement damage level, while Eurofer among them has the greatest effect in the flattering the heat production distribution in the test module. This and other favourable properties of Eurofer (like the well investigated behaviour of its mechanical properties under irradiation and its reduced activation) make it one of the most reasonable candidate materials for the reflector. We have selected it for the further, more detailed investigation.

With a 10 cm thick Eurofer reflector the spatial gradient along the deuteron beam direction (in which it has the maximum value) ranges from 18 to 20%/cm for the displacement rate and 4 to 13%/cm for the nuclear heating density. The influence on other neutronics parameters is shown in Figs. 37 to 41 and Table 6. In particular, this table shows that neutron and photon fluxes averaged over the HFTM volume increase by 20-40% due to the reflector. The displacement rate, sensitive mainly to the high energy neutron flux, increases by 8%, and the volume available for material testing at ≥ 20 dpa/fpy by 16%. Maximum changes up to 45%

are expected for the photon flux and up to 20% for the nuclear heating, which depends on both neutrons and photons. It is interesting to note that the reflector practically does not affect the hydrogen and helium generation in the HFTM. The reason is that the reflector, as shown in Fig. 42, returns neutrons practically only with energies below a few MeV, i.e., mostly below thresholds for (n,xp) and (n,xα) reactions. Anyhow the IFMIF neutron spectrum is harder than the spectrum in a fusion reactor, so that the gas production rate is sufficient and does not require additional enhancement.

Table 6 lists results obtained with two libraries, LANL and INPE. Their comparison shows that differences in the average responses due to the different libraries are near 10%. At the same time it is worthwhile to note that the relative changes of parameters due to the reflector (shown in parenthesis) do not depend on the evaluated data. This means that reflector effect is estimated rather reliable.

Table 6. Nuclear induced effects in HFTM with and without reflector.

Parameter	No Reflector		Reflector: Eurofer/10cm	
	LANL	INPE	LANL	INPE
Displacements per atom rate				
Average dpa-rate, 1/fpy	28.8	30.5	31.1 (+ 8 %)	33.6 (+ 8 %)
Volume (dpa-rate ≥ 50 1/fpy), cm^3	26	43	33 (+ 27 %)	58 (+ 35 %)
Volume (dpa-rate ≥ 40 1/fpy), cm^3	95	115	111 (+ 17 %)	140 (+ 22 %)
Volume (dpa-rate ≥ 20 1/fpy), cm^3	368	385	428 (+ 16 %)	458 (+ 19 %)
Heat Production				
Average Heating, W/cm^3	14.0	16.5	16.9 (+ 21 %)	19.7 (+ 19 %)
Volume (Heating ≥ 20 W/cm^3), cm^3	63	143	124 (+ 97 %)	226 (+ 58 %)
Volume (Heating ≥ 15 W/cm^3), cm^3	207	287	326 (+ 57 %)	413 (+ 44 %)
Volume (Heating ≥ 10 W/cm^3), cm^3	385	444	485 (+ 26 %)	496 (+ 2 %)
Hydrogen Production				
Average H-production, appm/fpy	1577	1742	1602 (+ 1.5 %)	1767 (+ 1.4 %)
Volume (H ≥ 2500 appm/fpy), cm^3	31.3	70.5	33.8 (+ 8.0 %)	72.3 (+ 2.5 %)
Volume (H ≥ 2000 appm/fpy), cm^3	116.3	162.5	121.8 (+ 4.7 %)	167.0 (+ 2.8 %)
Volume (H ≥ 1500 appm/fpy), cm^3	247.8	289.5	255.8 (+ 3.2 %)	300.0 (+ 3.2 %)
Helium Production				
Average He-production, appm/fpy	340	392	345 (+ 1.5 %)	396 (+ 1.0 %)
Volume (He ≥ 500 appm/fpy), cm^3	58.0	115.3	59.0 (+ 1.7 %)	117.0 (+ 1.5 %)
Volume (He ≥ 400 appm/fpy), cm^3	146.3	214.0	152.0 (+ 3.9 %)	218.5 (+ 2.1 %)
Volume (He ≥ 300 appm/fpy), cm^3	280.5	348.0	291.0 (+ 3.7 %)	358.0 (+ 2.9 %)
Neutron Flux				
Average n-flux, $10^{14}/cm^2/s$	5.86	5.93	7.05 (+ 21 %)	7.43 (+ 25 %)
Volume (n-flux ≥ $10\times10^{14}/cm^2/s$), cm^3	39	46	67 (+ 71 %)	80 (+ 74 %)
Volume (n-flux ≥ $8\times10^{14}/cm^2/s$), cm^3	105	111	157 (+ 50 %)	180 (+ 62 %)
Volume (n-flux ≥ $5\times10^{14}/cm^2/s$), cm^3	276	280	400 (+ 45 %)	436 (+ 56 %)
Gamma-ray Flux				
Average γ-flux, 10^{14} $/cm^2/s$	2.33	2.50	3.38 (+ 45 %)	3.59 (+ 44 %)
Volume (γ-flux ≥ $3\times10^{14}/cm^2/s$), cm^3	119	162	368 (+ 209 %)	404 (+ 149 %)
Volume (γ-flux ≥ $2\times10^{14}/cm^2/s$), cm^3	320	348	495 (+ 55 %)	498 (+ 43 %)
Volume (γ-flux ≥ $1\times10^{14}/cm^2/s$), cm^3	481	486	500 (+ 4 %)	500 (+ 3 %)

The 3-dimensional calculations providing the information on spatial distributions are very important for the optimization of the test module geometry and for reaching the desired damage levels in the tested materials. Since a convenient visualization of three dimensional results faces certain problems, we present them in two types of contour plots: (i) along three orthogonal planes of the main coordinate system (Fig. 37-41); (ii) along three parallel horizontal planes cutting the HFTM at different vertical levels (Fig. 43). These plots show that the spatial distributions of neutron induced effects, as expected already from the preliminary calculations [4], have shapes resembling half cylinders with axis along the horizontal direction and smoothed boundaries. The reflector stretches the cylinder in all directions to some extent. Nevertheless the spatial gradient still has its maximum value along the beam direction. It is seen that the 20×5×5 cm^3 box shape selected for the HFTM to have in this volume a displacement rate exceeding 20 dpa/fpy does not optimally fit the assessed 3-dimensional contour surfaces. As Fig. 43 shows, there is a 1 cm thick layer above (and equally below) the top surface (Y=2.5 cm) of the reference HFTM volume, in which the specified displacement production rate will be available. This means that by optimizing the geometrical configuration the volume for irradiation at ≥ 20 dpa/fpy can be increased by 23% (from 368 to 453 cm^3) and with a 10 cm thick Eurofer reflector by another 17% (up to 530 cm^3).

Besides rescattering the source neutrons into the HFTM, the reflector will absorb radiation that will result in heat generation. Table 7 shows the results of calculations for the reflector made of 10 cm thick Eurofer plates. As it is seen, the maximum averaged heat density and nuclear heating are expected in the top and bottom plates, and the minimum in the rear plate or in the medium flux test module. The total heat production amounts to near 26 kW in 14.5 l volume of the reflector. This heating power corresponds about 20% of the d-Li source radiation power.

Table. 7. Nuclear heating in the reflector made from Eurofer at full IFMIF performance.

Reflector' Part	Sizes (x×y×z), cm	Volume, cm^3	Density, g/cm^3	Heat Density, W/cm^3	Heating, kW
Top plate	20×10×15	3000	4.58	2.53	7.58
Bottom plate	20×10×15	3000	4.58	2.53	7.58
Left plate	10×25×15	3750	7.02	1.33	5.00
Right plate	10×25×15	3750	7.02	1.33	5.00
Rear plate (MFTM)	20×5×10	1000	6.24	0.54	0.54
Sum		**145000**		**1.77**	**25.7**

5.4 Neutronics evaluation of deployment scenarios

In the previous sections the detailed neutronics calculations for the full performance facility (two 40 MeV deuteron beams, total current 250 mA) have been described. During the IFMIF deployment phase or in a cost-reduced design, different operation scenarios are in principle foreseen [3]. We have studied the impact of two factors on the neutronics parameters: reduction of beam configuration/current and of deuteron incidence energy.

It is most likely that IFMIF will start to operate with one accelerator delivering one deuteron beam to the lithium target. At this first stage only 50 mA beam current will be available for a few years, followed by a stepwise increase up to 125 mA (see Starting Stage I and II in

Table 8). For the second stage we considered a 20×5 cm^2 beam footprint, the same as for the full performance, whereas at the first stage with small current two options for the beam configuration were investigated: Option 1 with the same footprint but low current density, 0.5 mA/cm^2; Option 2 with reduced beam footprint of 4×5 cm^2 (Fig. 44), resulting in to 2.5 mA/cm^2 current density, the same as foreseen for the full performance stage.

Table. 8. Scenarios of IFMIF concept deployment and main neutronics parameters (given the accelerated deuteron energy of 40 MeV).

Deployment Stage	Starting I		Starting II	Full Performance
	Option 1	Option 2		
Beam/Accelerator Options				
# Beams/Accelerators	1	1	1	2
Each beam current, mA	50	50	125	125
Beam power, MW	2	2	5	10
Beam foot print (width × height), cm	20 × 5	4 × 5	20 × 5	20 × 5
Beam density, mA/cm^2	0.5	2.5	1.25	2.5
Radiation induced effects averaged over HFTM volume (500 cm^3)				
n-flux, $10^{14}/cm^2/s$	1.2	1.3	2.9	5.8
γ-flux, $10^{14}/cm^2/s$	0.45	0.52	1.1	2.2
Displacement production, dpa/fpy	5.6	6.1	14	28
Volume (dpa > 20/fpy), cm^3	-	39	79	358
Volume (dpa > 40/fpy), cm^3	-	4	-	70
H production, appm/fpy	306	330	765	1517
He production, appm/fpy	66	71	164	327
Nuclear heating, W/cm^3	2.7	3.1	6.8	13.3

The results of the calculations are summarised in Table. 8. They generally show that the irradiation neutronics parameters averaged over the 500 cm^3 HFTM volume are proportional to the beam current and practically do not depend on the current density. On the other hand, the volume available for material testing at some minimum damage level, e.g. ≥ 20 dpa/fpy, depends on both the current and density. For example, if users would like to have the relatively higher rate of damage accumulation at the expense of volume at the first starting stage, the reduced beam footprint configuration with higher current density should be selected. The higher spatial gradient can be expected in this case as well.

The IFMIF strategy foresees the variation of the deuteron energy delivered to the Li target from 32 to 40 MeV. The accelerated energy of 40 MeV will provide the most intense irradiation, whereas lower energies will help to investigate the dependence of damage effects on neutron spectra. To evaluate such scenarios the nuclear responses were calculated for the full performance beam configuration also at energies 32 and 36 MeV. The results obtained for the neutronics parameters averaged over the HFTM volume are shown in Fig. 45. It shows that the 25% increase of deuteron energy from 32 to 40 MeV will result in 22% increase of the neutron flux and 30% in the average neutron energy. These two factors will increase the nuclear responses in the HFTM by 40 to 90%. The most significant increase is observable in gas production processes since the related cross sections are sensitive to high energy neutrons. Thus the variation of deuteron energy will change the ratio between displacement and gas transmutation rates.

Summary and Conclusions

The development of IFMIF requires a set of computational tools and input data for performing neutronics analyses and predicting irradiation parameters with desirable completeness and accuracy for the design and engineering assessment of the project and its modifications. One main outcome of the present work is the M^{C}DeLicious code which is able to simulate the IFMIF neutron source term with highest accuracy and takes into account all open reaction channels. This is accomplished by using d-Li reaction cross sections evaluated at INPE in collaboration with FZK. This approach is obviously more advanced and flexible than the codes M^{C}DeLi or MCNPX, which use built-in analytical semi-empirical models for the Li(d,xn) reaction cross section, since it opens the possibility for further improvements of the IFMIF source term prediction as soon as updated and validated d-Li data become available.

The developed M^{C}DeLicious code and the new d-Li evaluated library have been validated against compiled available experimental data on the differential neutron yield from deuteron bombarded thick lithium targets. This comparison has indeed shown that M^{C}DeLicious predicts the spectral and angular neutron yields better than M^{C}DeLi or MCNPX do.

The cross sections from the latest versions of the INPE and LANL evaluations for the transport of neutrons with energies up to 50 MeV and assessment of nuclear responses were processed. The intercomparison of processed evaluated cross sections has shown satisfactory agreement, thus proving that reliable nuclear data for IFMIF neutronics calculations do exist.

Using the M^{C}DeLicious code with INPE and LANL evaluated data, a comprehensive neutronics characterisation has been performed for the IFMIF lithium target, its backplate and the high flux test module. The energy deposition, neutron and photon fluxes, gas and heat production, and displacement damage rate have been assessed for IFMIF at full performance and intermediate deployment stages. The analyses of the neutron spectral distribution and gas-to-displacement production ratio have shown that IFMIF can sufficiently well simulate the D-T fusion irradiation environment.

Three dimensional analysis of spatial distributions for the neutron induced effects inside the HFTM results in an assessment of the actual shape and the irradiation volume in which specified dpa rates, e.g. more than 20 dpa/fpy in steel, can be reached. This analysis has shown that further design optimisation of the reference 500 cm^3 test module could increase the volume available for material irradiation tests.

The idea of using a reflector around the HFTM to reach higher irradiation levels and lower spatial gradients has been carefully investigated with respect to selection of reflector material and thickness. It was found that 10 cm Eurofer plates surrounding the HFTM on all sides except the neutron entry side will increase the irradiation volume and at the same time decrease the spatial gradients of dpa rate and nuclear heat release by ≈10%.

Acknowledgment

This work has been performed in the framework of the nuclear fusion programme of Forschungszentrum Karlsruhe and is supported by the European Union within the European Fusion Technology Programme.

References

1. H. Matsui et al. IFMIF Status and Perspectives. 10th International Conference on Fusion Reactor Materials (Baden-Baden, October 2001)
2. M. Martone (Ed.). IFMIF – International Fusion Materials Irradiation Facility Conceptual Design Activity – Final Report. ENEA Frascati Report, RT/ERG/FUS/96/11 (December, 1999)
3. IFMIF Technical Meeting on Test Facilities/Users System (Karlsruhe, 22-24 October 2001)
4. E. Daum, U. Fischer, A.Yu. Konobeev et al. Neutronics of the High Flux Test Region of the International Fusion Materials Irradiation Facility (IFMIF). Report FZKA 5868, Karlsruhe, 1997
5. P.P.H. Wilson. Neutronics of the IFMIF neutron source: Development and Analysis. Report FZKA 6218, Karlsruhe 1999
6. U. Fischer, V. Heinzel, S. Simakov, U. v. Möllendorff. Neutronic optimisation of the high flux test module of the International Fusion Material Irradiation Facility (IFMIF). Jahresrtagung Kerntechnik 2001, Dresden, May 2001. Bonn: INFORUM GmbH, 2001, p. 581
7. U. Fischer, S.P. Simakov et al. Neutronics and Nuclear Data for the IFMIF neutron source. Proc. 6th Int. Symp. on Fusion Nuclear Technology (ISFNT-6), San Diego, Apr, 2002
8. V. Heinzel, B. Dolensky, U. Fischer et al. Design Optimization of the IFMIF High Flux Test Module. Proc. 10th International Conference on Fusion Reactor Materials (Baden-Baden, October 2001)
9. S.P. Simakov, U. Fischer, U. von Möllendorff et al. Advanced Monte Carlo procedure for the IFMIF d-Li neutron source term based on evaluated cross section data. 10th International Conference on Fusion Reactor Materials (Baden-Baden, October 2001)
10. S.P. Simakov, U. Fischer, U. von Möllendorff. Unpublished report, 2000
11. J.F. Briesmeister (Ed), MCNP – A General Monte Carlo N-Particle Transport Code, Version 4b, Los Alamos National Laboratory Report LA-12625-M (1997).
12. J.F. Briesmeister(Ed.). MCNPTM – A General Monte Carlo N-Particle Transport Code, Version 4C. Report LA-13709-M, Los Alamos National Laboratory, 2000
13. L.S. Waters (Ed), MCNPX™ User's Manual, version 2.1.5, available from http://mcnpx.lanl.gov
14. J.F. Ziegler et al. The Stopping and Range of Ions in Solids, Pergamon Press, 1985
15. A.Yu. Konobeev, Yu.A. Korovin, P.E. Pereslavtsev et al. Development of methods for calculation of n+Li and d+Li cross sections for energies up to 50 MeV. Nucl. Sci. and Eng., 2001, v. 139, p. 1
16. R.E. MacFarlane, D.W. Muir, R.M. Boicourt. NJOY99.00 – Code System for Producing Pointwise and Multigroup Neutron and Photon Cross Sections from ENDF/B Data. RSICC Code Package PSR-480, Oak Ridge, 1999
17. V.K. Daruga, V.G. Dvukhsherstnov, V.A. Dulin et al. Li + He^4, Li + H^2, Li + H^1 reactions as cyclotron sources of fast neutrons. Atomnaya Energiya, 1968, v. 24, No. 1, p. 71; V.K. Daruga and N.N. Krasnov. Production of strong, high-energy neutron fluxes in a cyclotron by irradiating thick lithium and beryllium targets with 22-MeV deuterons. Atomnaya Energiya, 1971, v. 30, No. 4, p. 399
18. K.A. Weaver, J.D. Anderson, H.H. Barschall, J.C. Davis. Neutron spectra from deuteron bombardment of D, Li, Be and C. Nucl. Sci. & Eng., 1973, v. 52, p. 35;

K.A. Weaver. Neutrons from deuteron bombardment of light nuclei. Report UCRL-51310, Livermore Nat. Lab., 1972
19. A.N. Goland, C.L. Snead, D.M. Parkin, R.B. Theus. Use of Li(d,n) neutrons for simulation of radiation effects in fusion reactors. IEEE Transactions on Nuclear Science, 1975, v. NS-22, p. 1776
20. H.I. Amols, M. Awschalon et al. Physical characterization of neutron beams producted by protons and deuterons of various energies bombarding beryllium and lithium targets of several thicknesses. Report FERMILAB-Pub-76/102-EXP, Fermi Laboratory, Batavia, 1976; H.I. Amols, J.F. Dicello, M. Awschalon et al. Physical characterization of neutron beams producted by protons and deuterons of various energies bombarding beryllium and lithium targets of several thicknesses. Med. Phys., 1977, v. 4, p. 486
21. C.E. Nelson, F.O. Purser, P. Von Behren and H.W. Newson. Neutron spectra from deuteron and proton bombardment of thick lithium targets. Report NBIR-77-1279, 1977, p. 1. National Bureau of Standards, Washington, DC; Report BNL-NCS-50681, Brookhaven National Laboratory, Upton, NY, 1979
22. M.A. Lone. Neutron spectral distribution from proton and deuteron bombardment of thick Li & Be targets at 14.8, 18 &23 MeV. Report NBIR-77-1279, 1977, p. 5. National Bureau of Standards, Washington, DC; M.A. Lone, C.B. Bigham, J.S. Fraser et al. Thick target neutron yields and spectral distributions from the ^{7}Li($^{d}_{p}$,n) and ^{9}Be($^{d}_{p}$,n) reactions. Nucl. Instr. & Meth., 1977, v. 143, p. 331
23. M.J. Saltmarsh, C.A. Ludemann, C.B. Fulmer and R.C. Styles. Neutron Yields and Dosimetry for Be(d,n) and Li(d,n) Neutron Sources at E_d = 40 MeV. Report NBIR-77-1279, 1977, p. 24. National Bureau of Standards, Washington, DC; M.J. Saltmarsh, C.A. Ludemann, C.B. Fulmer and R.C. Styles. Characteristics of an intense neutron source based on the d+Be reaction. Nucl. Instr. & Meth., 1977, v. 145, p. 81
24. D.L. Johnson, F.M. Mann, J.W. Watson et al. Measurement and calculations of neutron spectra from 35 MeV deuterons on thick lithium for FMIT facility. Journal of Nucl. Mater. 1979, v. 85&86, p. 467; D.L. Johnson, F.M. Mann, J.W. Watson et al. Thick target neutron yields and spectra from Li(d,n) reaction at 35 MeV. Report BNL-NCS-51245, 1980, p. 99. Brookhaven National Laboratory, Washington, DC
25. M. Sugimoto. Double differential neutron yields from Li(d,n) experiments. JAERI, private communication, 1995
26. F.M. Mann, F. Schmittroth, L.L. Carter. Neutrons from d+Li and the FMIT irradiation environment. Report HEDL-TC-1459, Richland, 1981
27. Yu.A. Korovin, A.Yu. Konobeev, P.E. Pereslavtsev et al. Evaluation and test of nuclear data for investigation of neutron transport, radiation damage and processes of activation and transmuation in materials irradiated by intermediate and high energy particles. Proc. Int. Conf. on Nuclear Data for Scince and Technology, SIF, Bologna, 1997, p. 851
28. Yu.A. Korovin, A.Yu. Konobeev, P.E. Pereslavtsev et al. Evaluated nuclear data files for accelerator driven systems and other intermediate and high energy applications. Nucl. Instr. and Meth., 2001, v. A463, p. 544
29. M.B. Chadwick, P.G. Young et al. Cross-Section Evaluations to 150 MeV for Accelerator-Driven Sytems and Implementation in MCNPX. Nucl. Sci. Eng. 131 (1999), 293
30. J.H. Hubbell, W.J. Veigele et al. Atomic Form Factors, Incoherent Scattering Functions, and Photon Scattering Cross Sections. J. Phys. Chem. Ref. Data, 1975, v. 4, p. 471

31. M.T. Robinson. in Nuclear Fusion Reactors. British Nuclear Energy Society, London, 1970, p. 364
32. L.R. Greenwood and R.K. Smither. SPECTER: Neutron Damage Calculations for Materials Irradiations. Report ANL/FPP/TM-197, Argone National Laboratory, 1985
33. Handbook on photonuclear data for applications. Cross-sections and spectra. Report IAE-TECDOC-1178, IAEA, Vienna, 2000
34. M.B. Chadwick, P.G. Young et al. Photonuclear physics in radiation transport: I. Cross-sections and spectra photonuclear cross-section evaluations to 150 MeV. Report LAUR-02-824, Los Alamos, 2002; submitted to Nucl. Sci. Eng. 2002
35. U. Fischer, D. Leichtle, H. Tsige-Tamirat. Neutronics characteristics of a solid breeder blanket for a fusion power demonstration reactor. Jahrestagung Kerntechnik 1999, Karlsruhe, May 1999. Bonn: INFORUM GmbH, 1999, p. 553
36. S. J. Zinkle et al. Scientific and engineering advances from fusion materials R&D. Proc. 10th International Conference on Fusion Reactor Materials (Baden-Baden, October 2001)

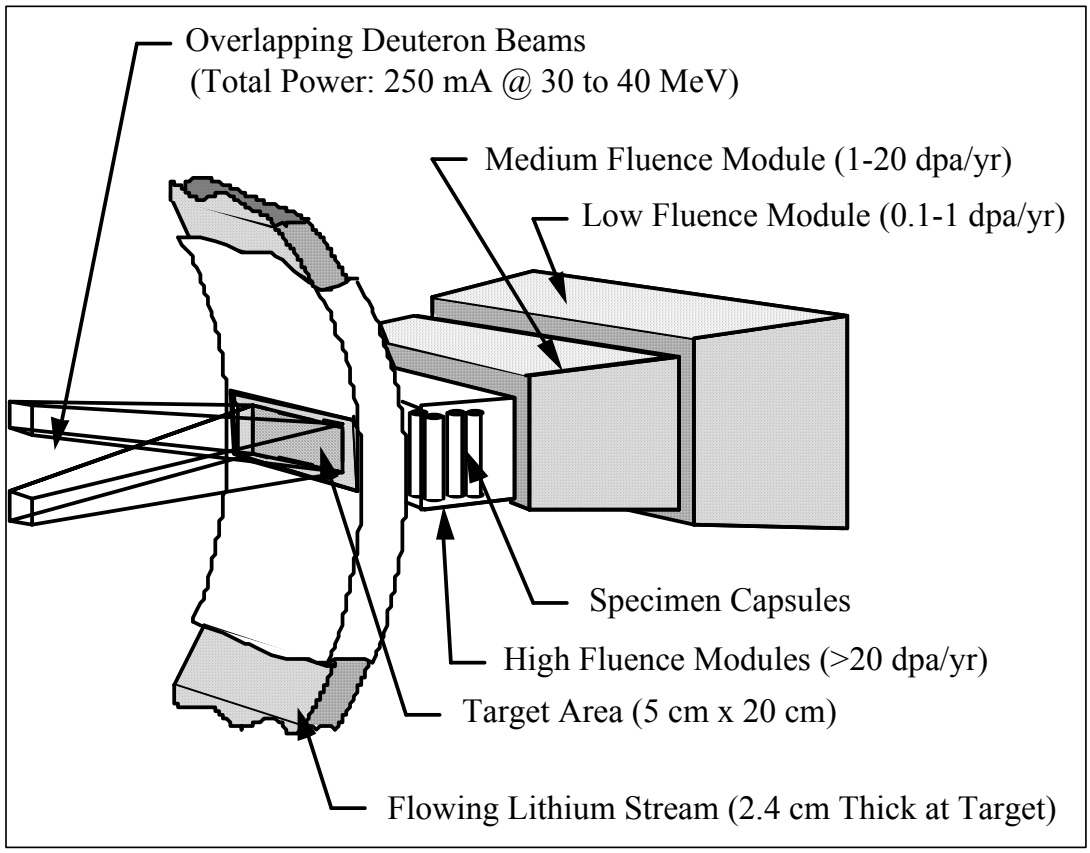

Fig.1 Schematic view of the target and test modules configuration

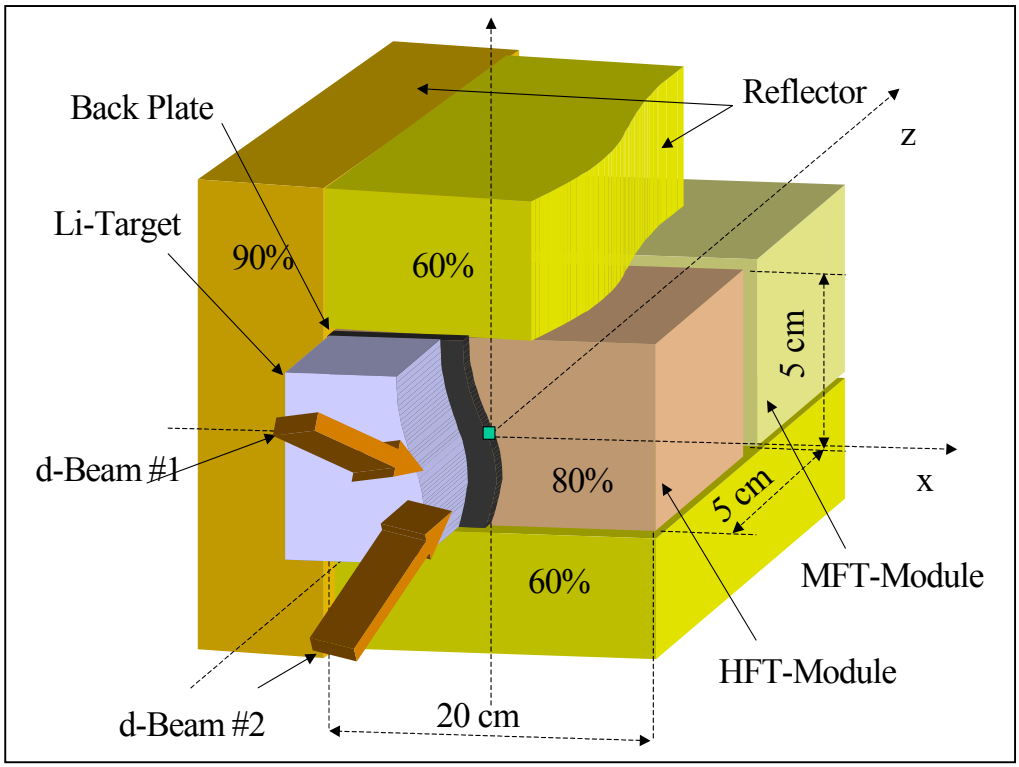

Fig. 2. Geometry and material distribution model for the Monte Carlo simulation: X-axis - horizontal direction; Y-axis - vertical direction; Z-axis - forward direction away from the target.

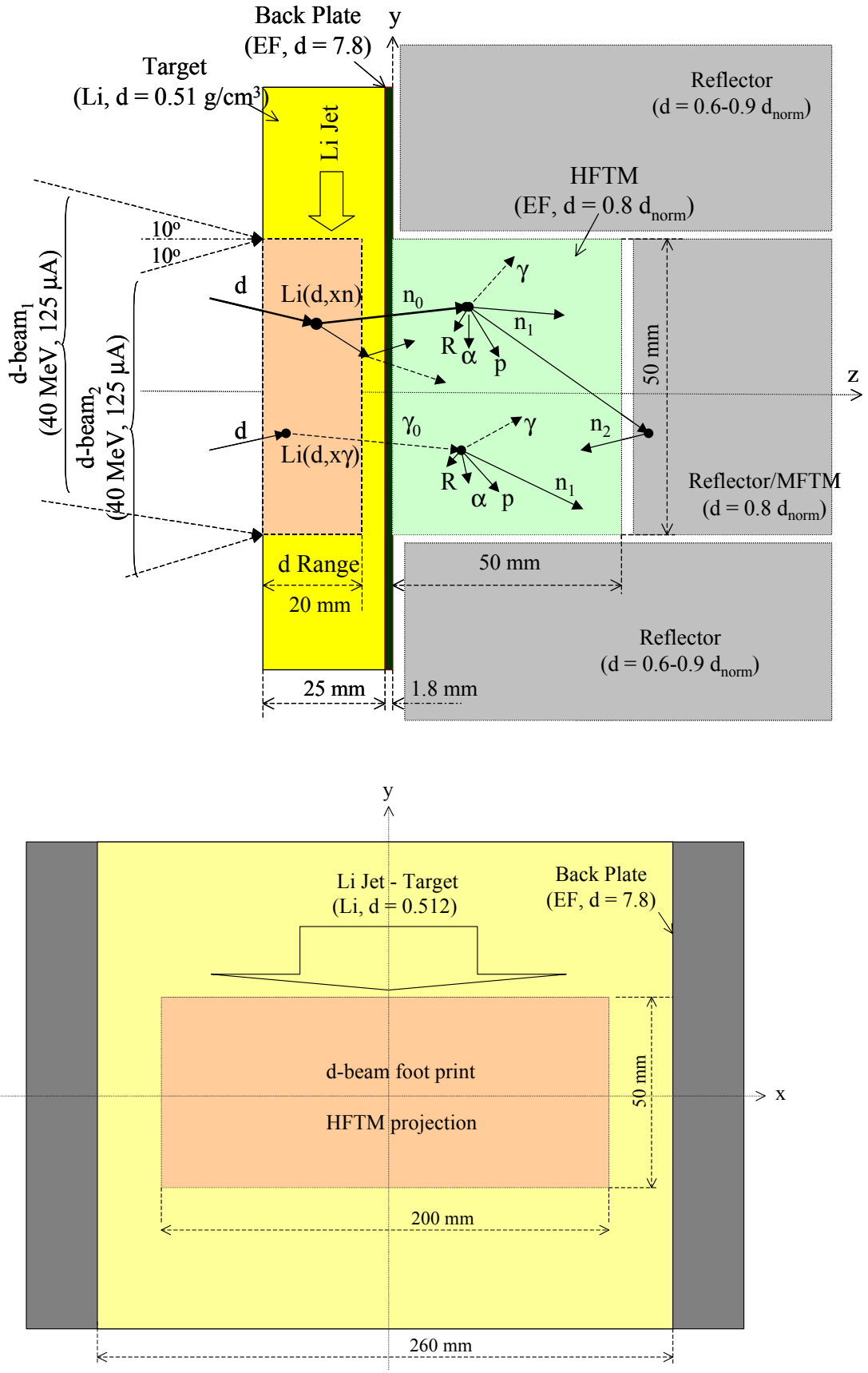

Fig. 3. Configuration and basic physical processes in the lithium target and test modules: top - side view, bottom - front (beam direction) view.

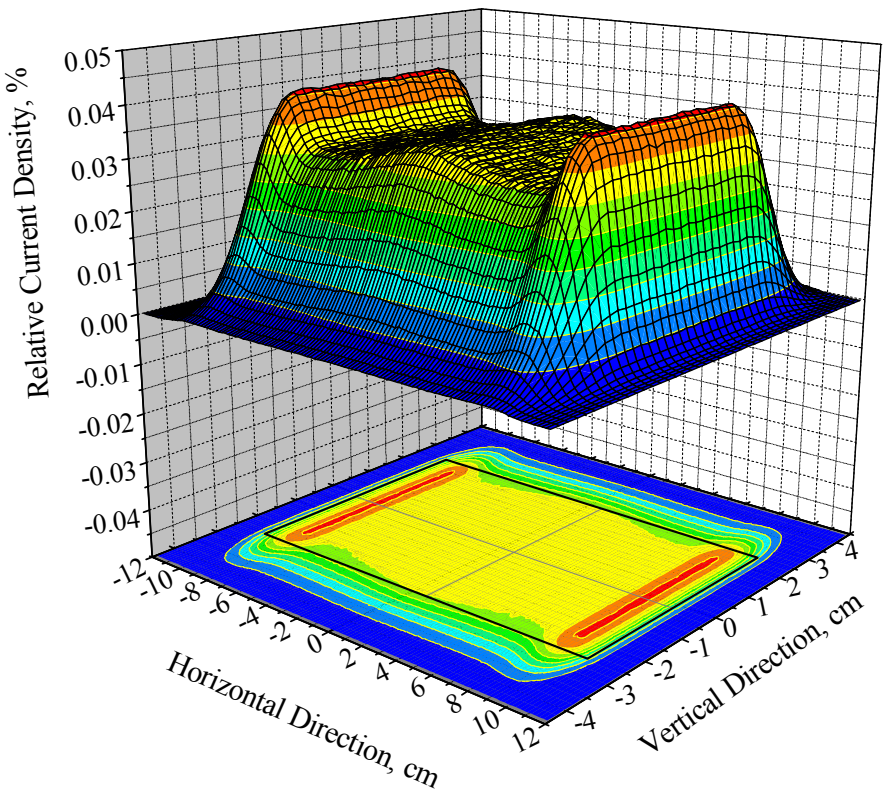

Fig. 4. Three-dimensional (top) and contour plot (bottom) presentation of the IFMIF deuteron beam profile. The box on the projection plane shows the front plate contour (20×5 cm^2) of the HFTM.

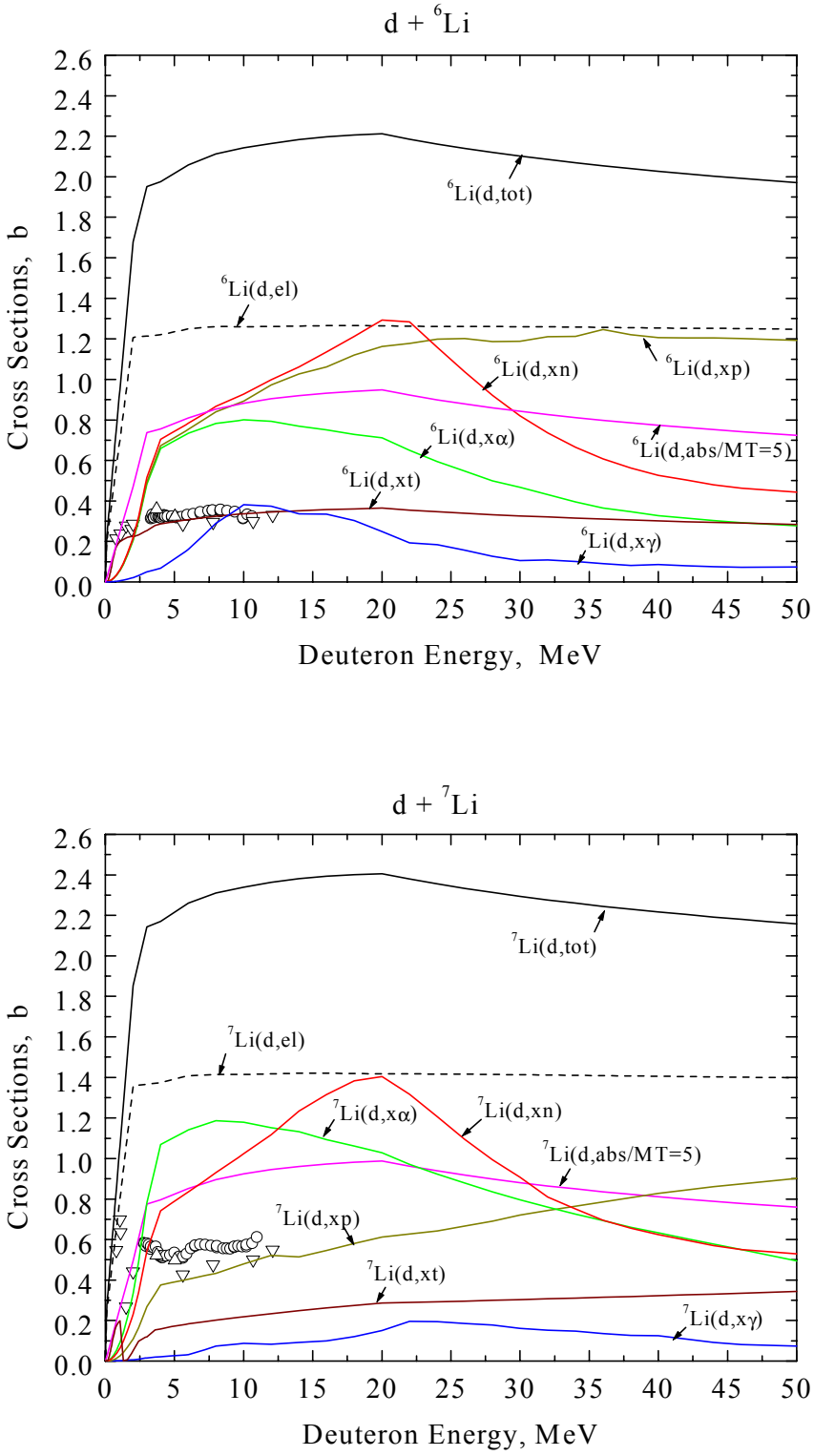

Fig. 5. Cross sections of deuteron interaction with ^{6}Li (top) and ^{7}Li (bottom): symbols – experimental data for (d,xn) reaction, curves – INPE evaluation.

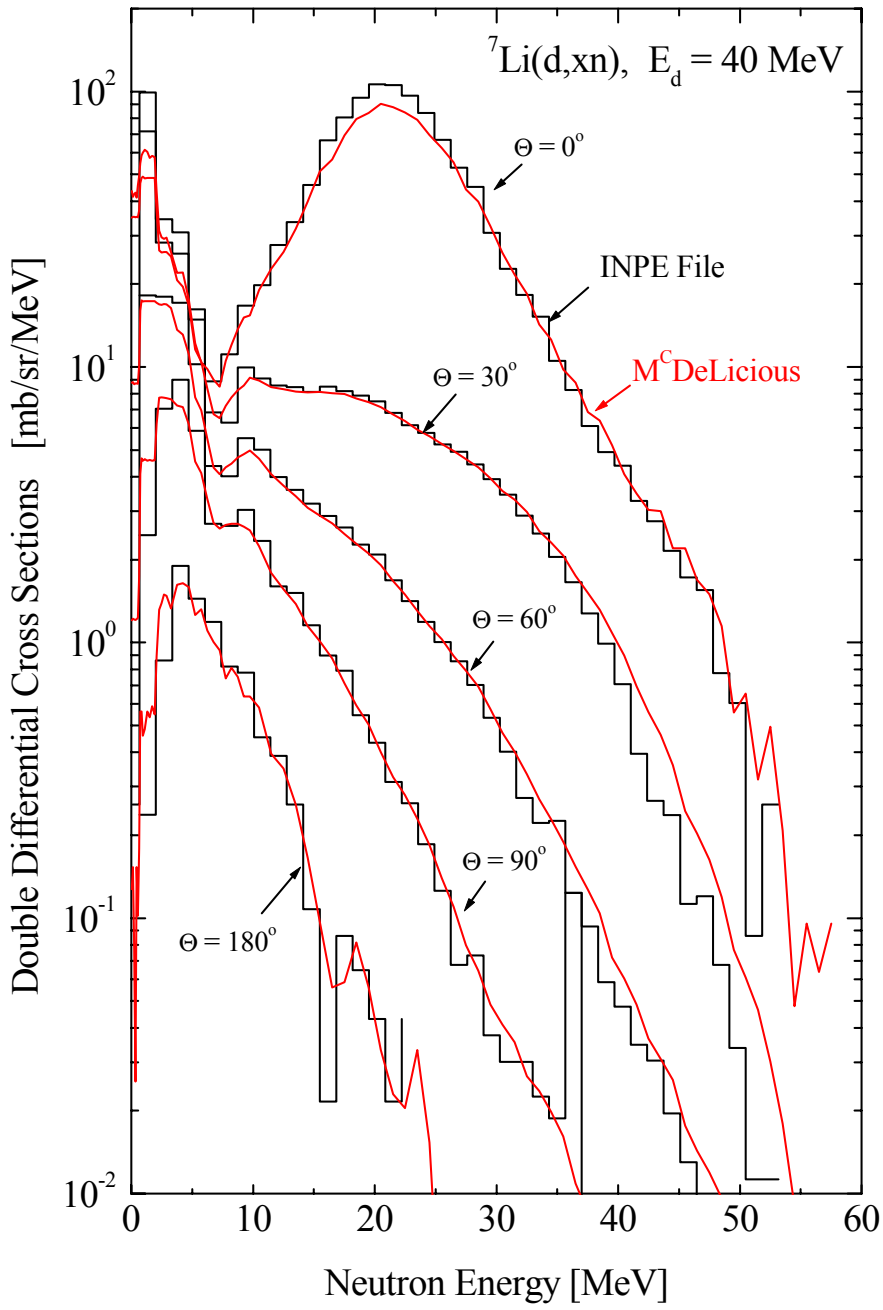

Fig. 6. Double differential cross sections of ^{7}Li(d,xn) reaction at E_d = 40 MeV: histogram – extracted from file INPE, smooth red curve – M^{C}DeLicious results with data from INPE evaluation.

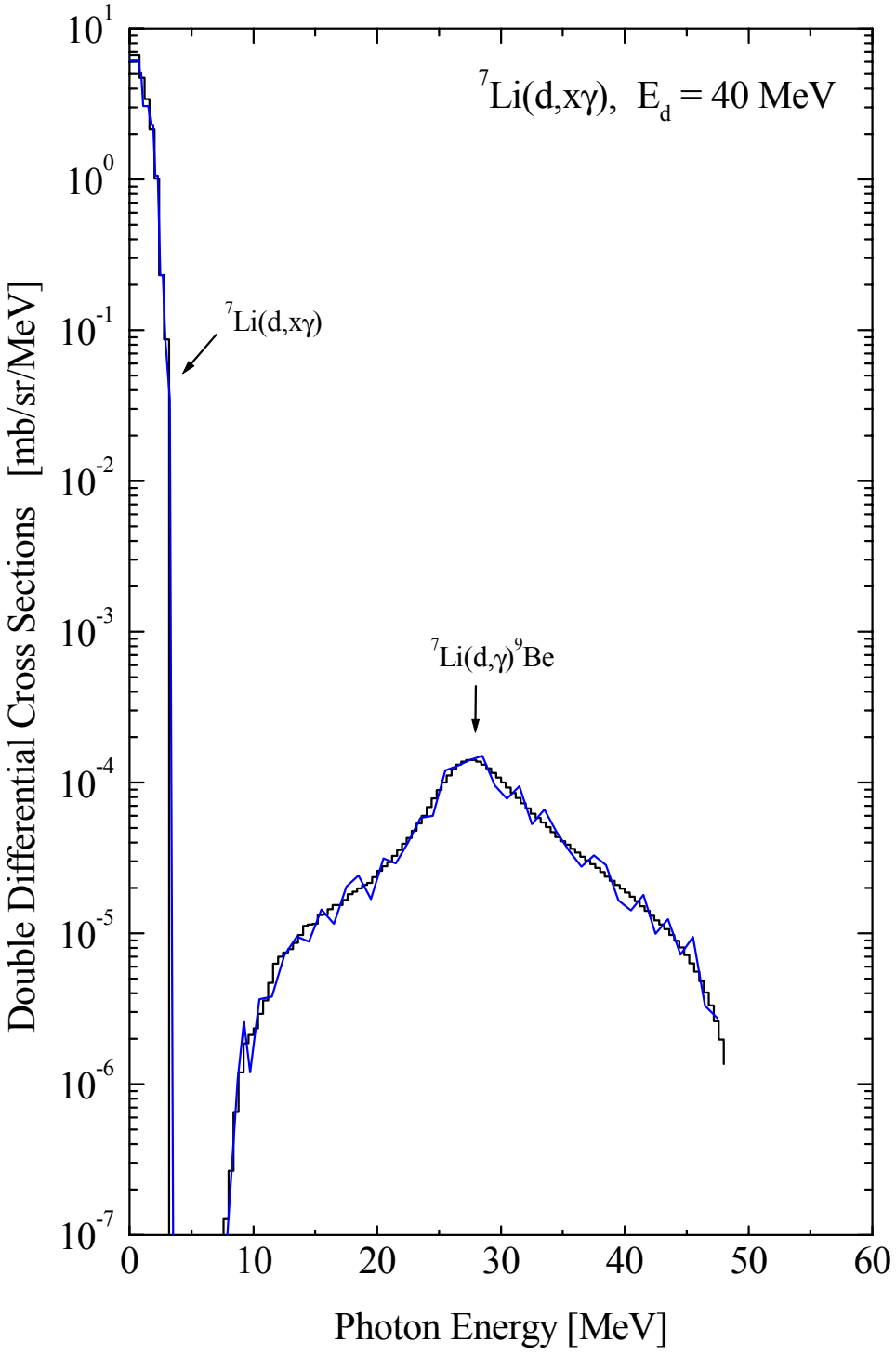

Fig. 7. Double differential cross sections of ^{7}Li(d,xγ) reaction at E_d = 40 MeV: histogram – extracted from file INPE, smooth blue curve – M^{C}DeLicious results with data from INPE evaluation.

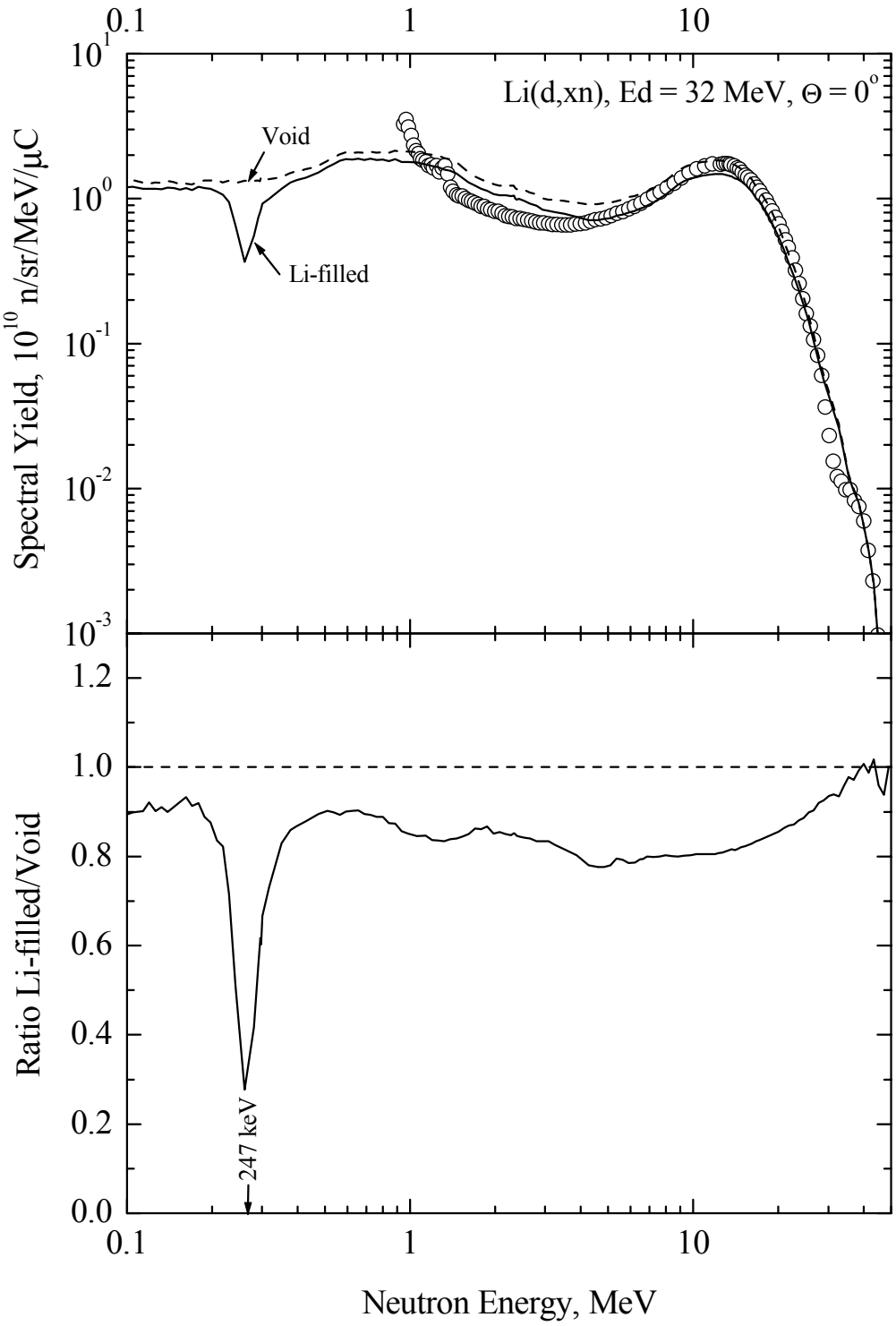

Fig. 8. Top - neutron spectra from Li target at E_d = 32 MeV in forward direction. Symbols – experiment [25], solid curve – calculated with the target cell (∅4×4cm) filled with lithium at normal density, dashed curve – void target cell.
Bottom – ratio of the two calculated spectra.

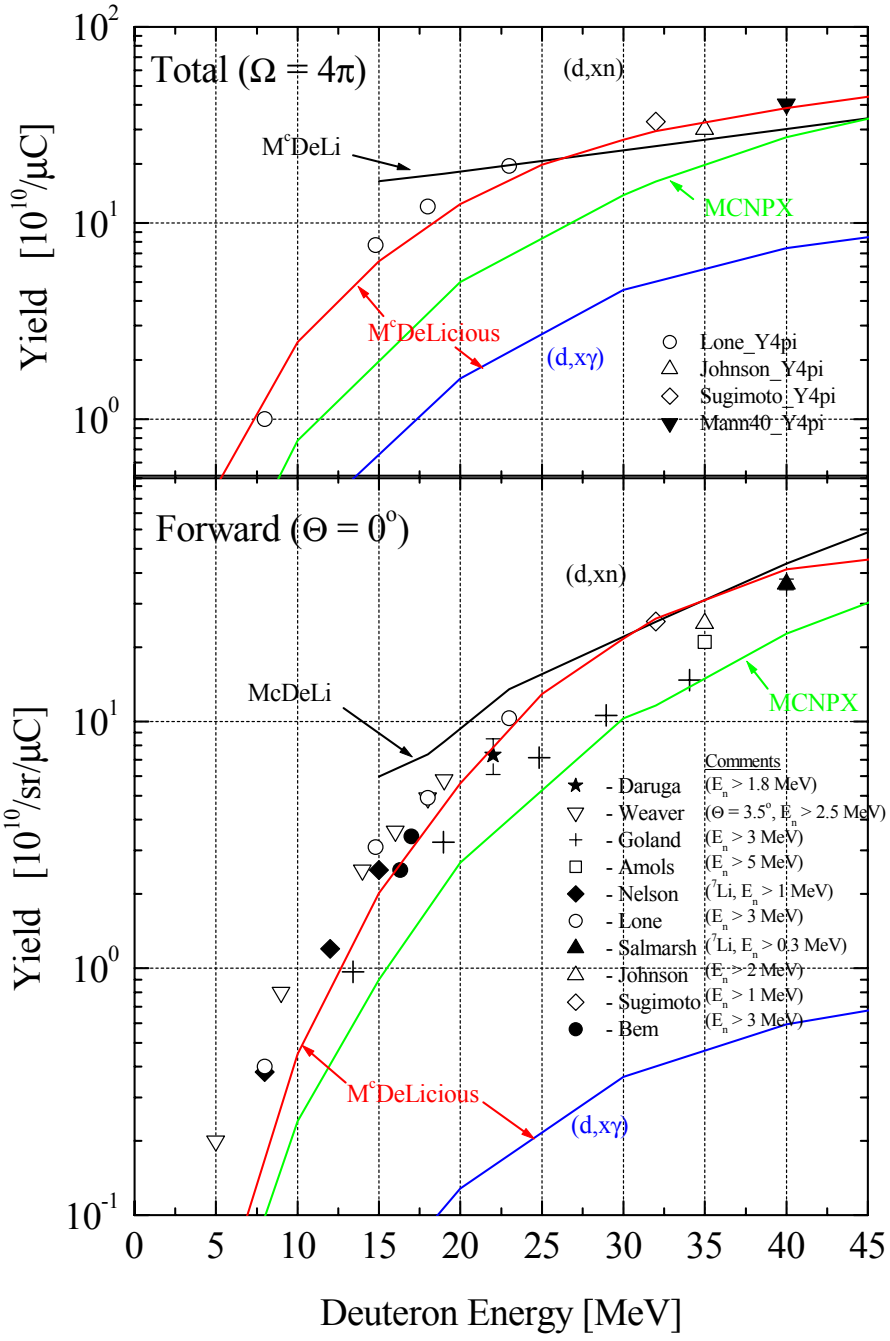

Fig. 9. Total (top) and forward direction (bottom) neutron and photon yields from thick lithium target versus the energy of bombarding deuterons. Symbols: experiment [17-25], curves: black – M^{C}DeLi, red/blue - M^{C}DeLicious (neutron/γ-ray yield), green – MCNPX.

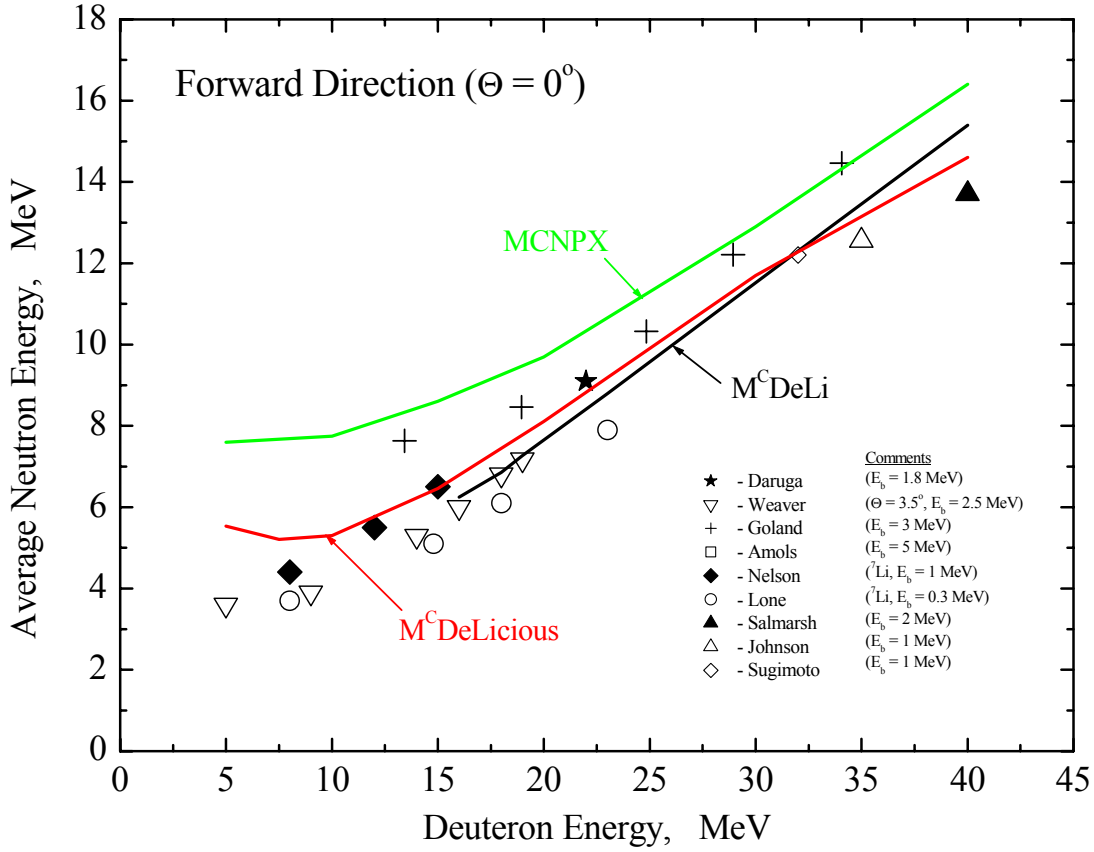

Fig. 10. Average energy of neutrons emitted in the forward direction as function of deuteron energy. Symbols – experimental data, black curve – M^{C}DeLi, red – M^{C}DeLicious, green - MCNPX.

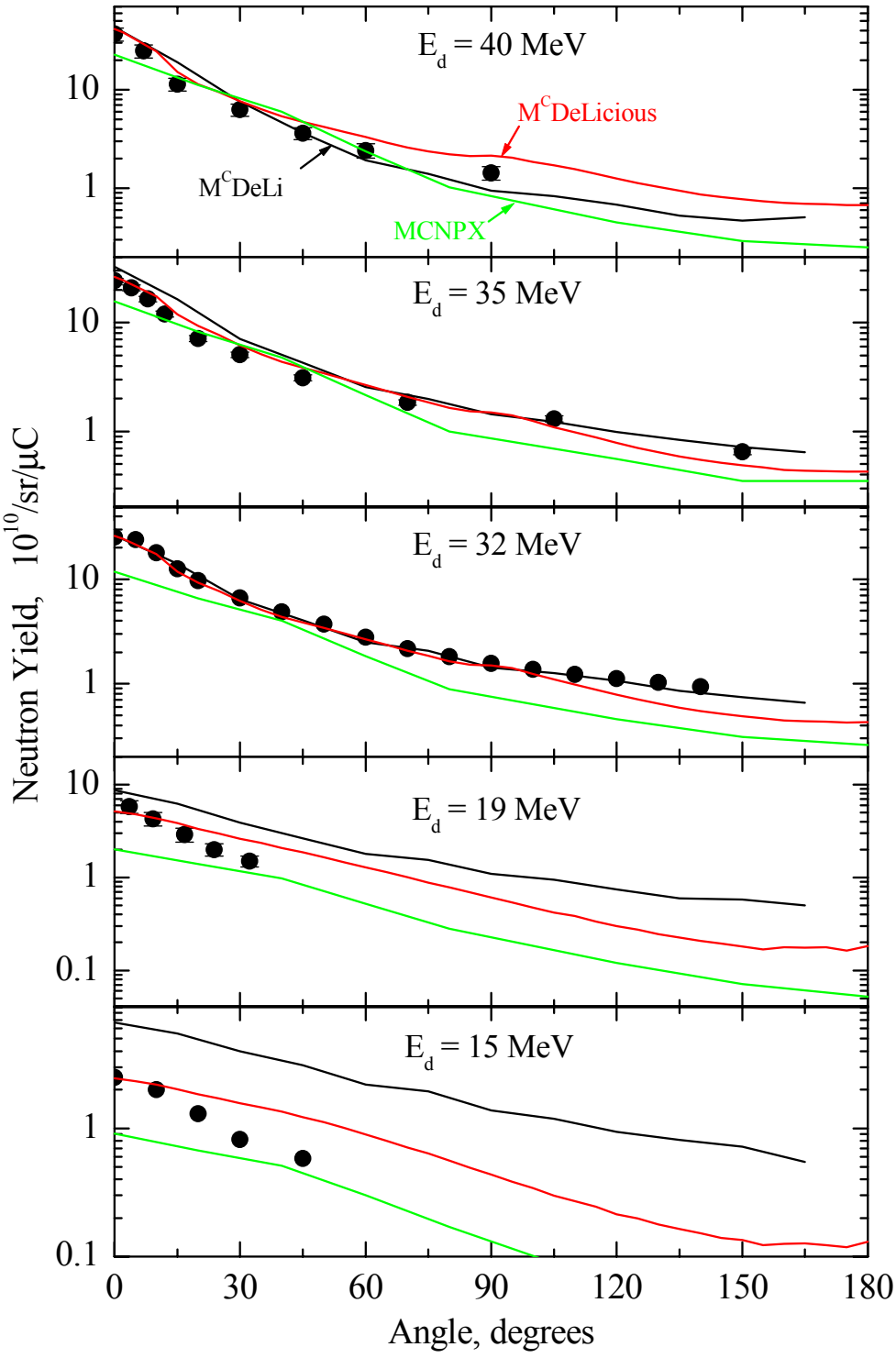

Fig. 11. Angular distributions of neutron yield from thick Li-target at different deuteron energies. Symbols – experimental data (at 40 MeV – [23], 35 MeV – [24], 32 MeV – [25], 19 MeV – [18], 15 MeV – [21]). Curves – M^{C}DeLi (black), M^{C}DeLicious/INPE (red), MCNPX (green).

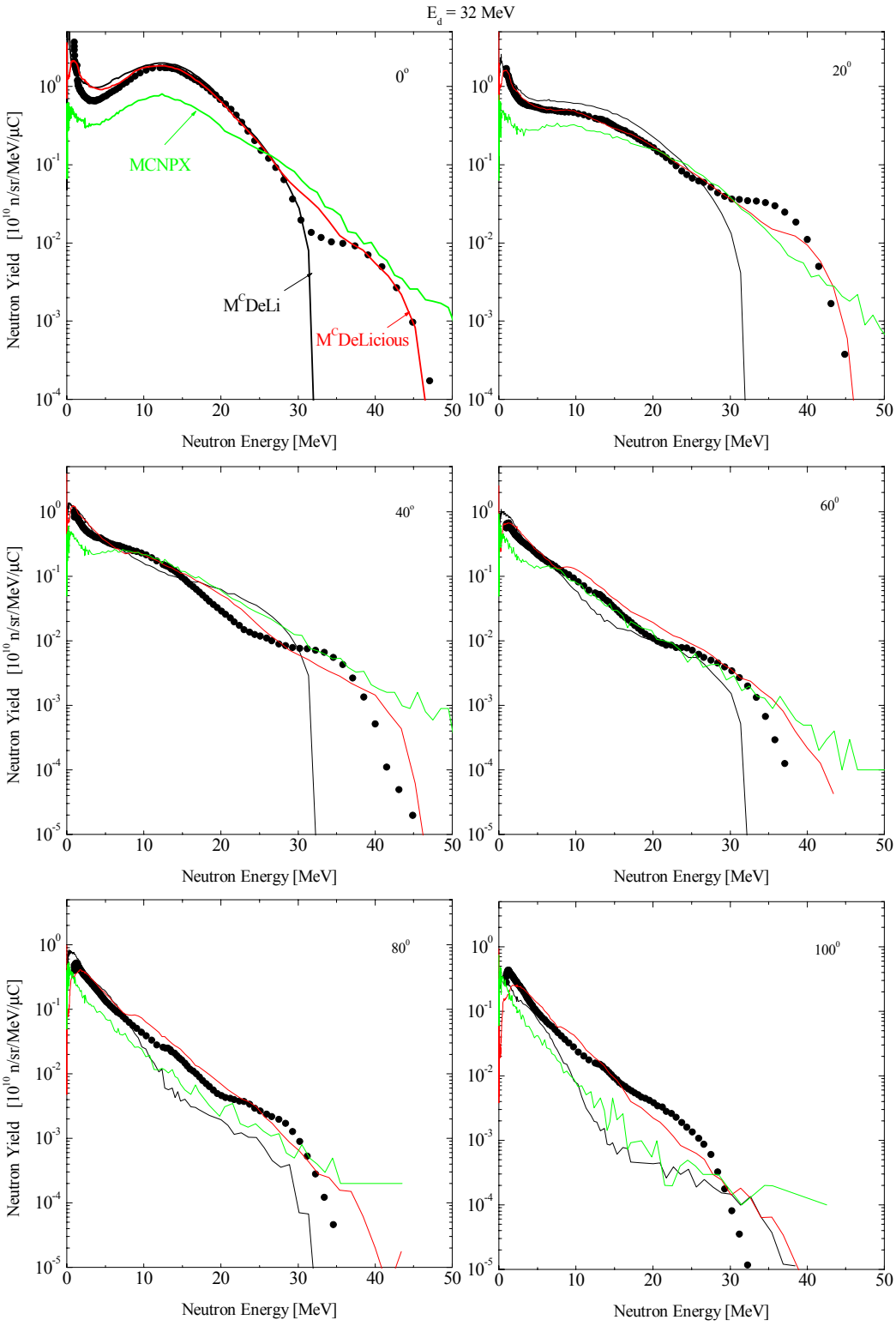

Fig. 12. Neutron energy spectra at different emission angles and deuteron energy 32 MeV. Symbols – experiment [25], black curve - M^{C}DeLi, red - M^{C}DeLicious/INPE, green - MCNPX.

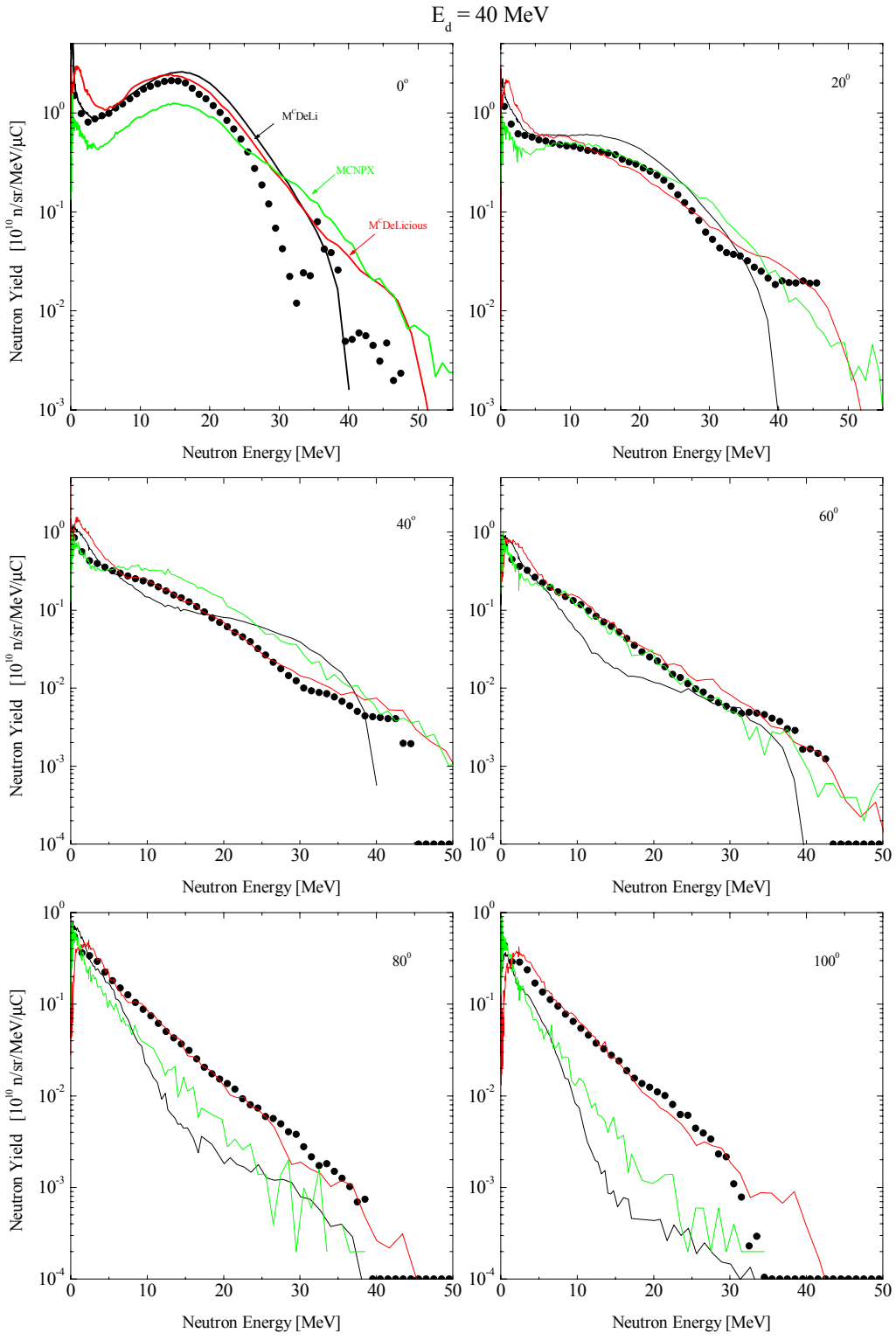

Fig. 13. Neutron energy spectra at different emission angles and deuteron energy 40 MeV. Symbols – experiment [26], black curve - M^{C}DeLi, red curve - M^{C}DeLicious/INPE, green - MCNPX.

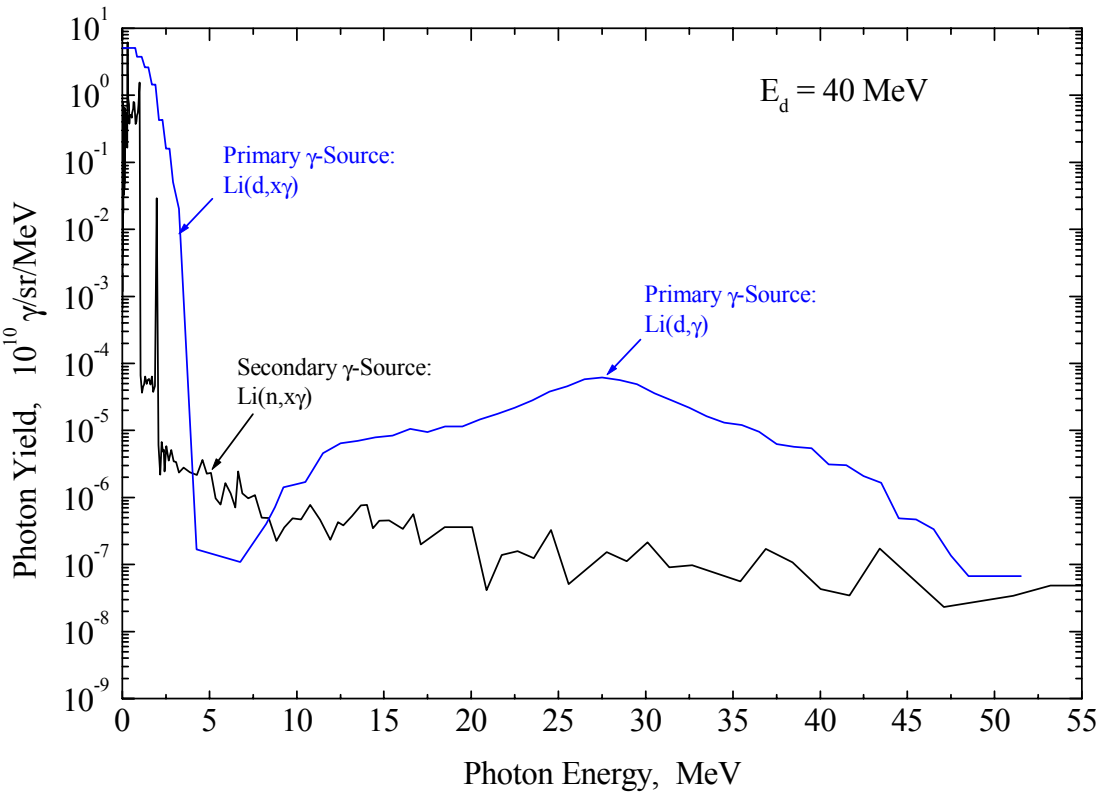

Fig. 14. Photon spectral yield from a thick lithium target at 40 MeV deuteron energy. Results of M^{C}DeLicious calculations: blue curve - primary yield from Li(d,xγ) reaction, black curve - secondary yield from neutron inelastic scattering on Li target (∅4×4cm), i.e. Li(n,xγ) reaction.

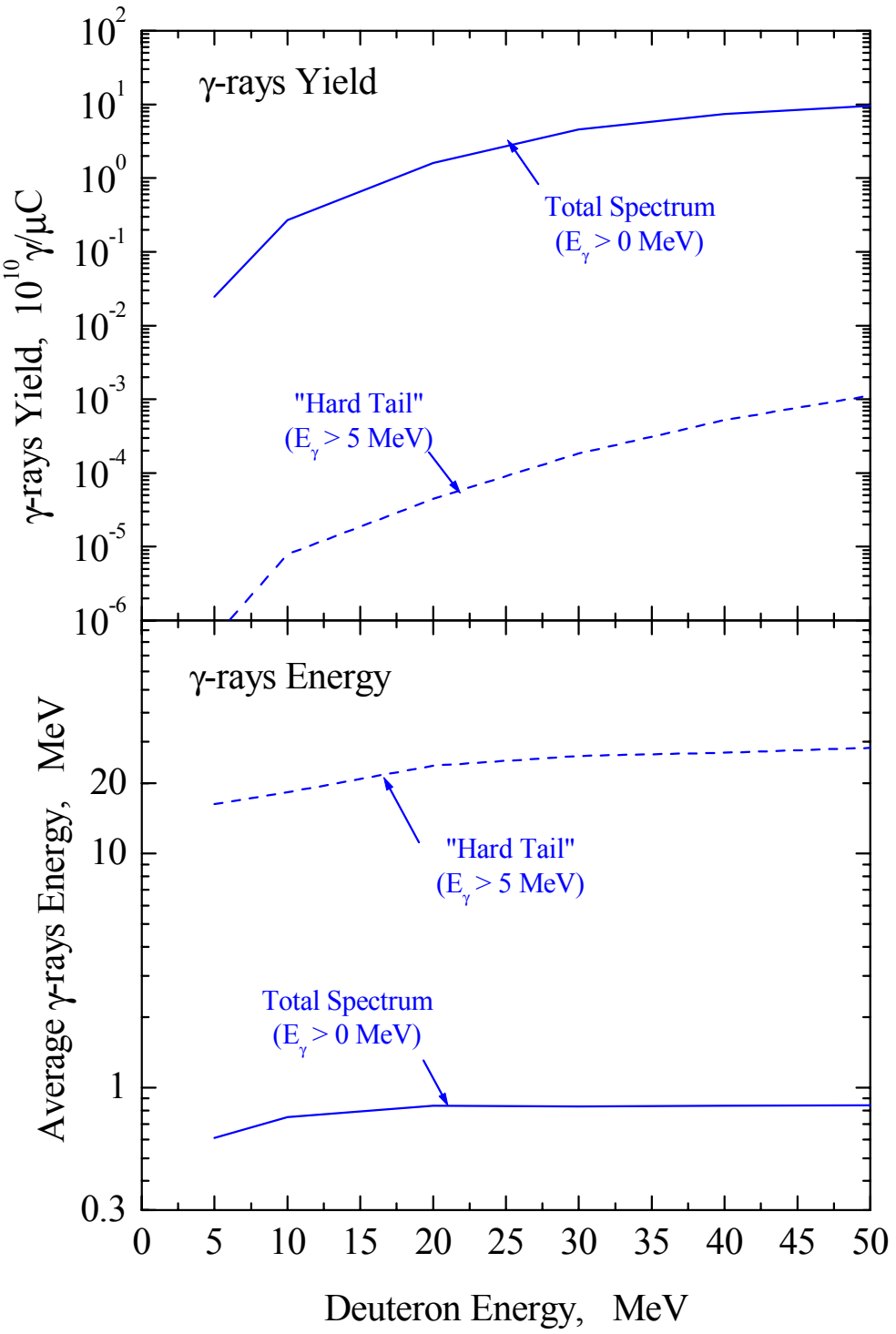

Fig. 15. Angle integrated yield (top) and average energy (bottom) of photons emitted from the thick lithium target versus the energy of bombarding deuterons, calculated with M^{C}DeLicious: solid curve - integrated over the whole spectrum, dashed – over the high energy part ($E_\gamma > 5$ MeV).

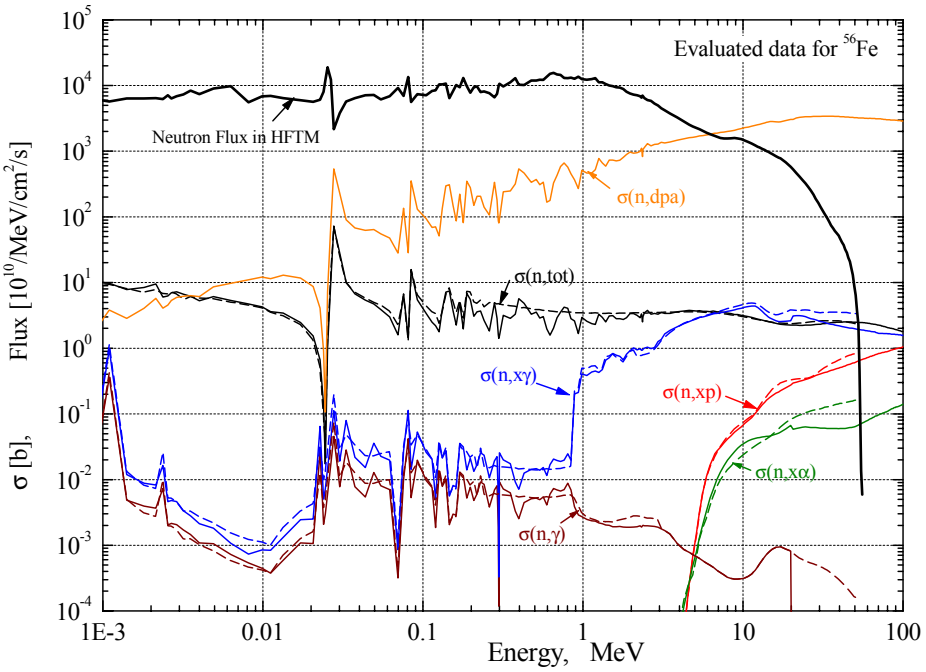

Fig. 16. Neutron reaction cross sections for ^{56}Fe as evaluated by LANL (solid line) and INPE (dashed). Thick line shows the IFMIF neutron spectal flux averaged over the HFTM.

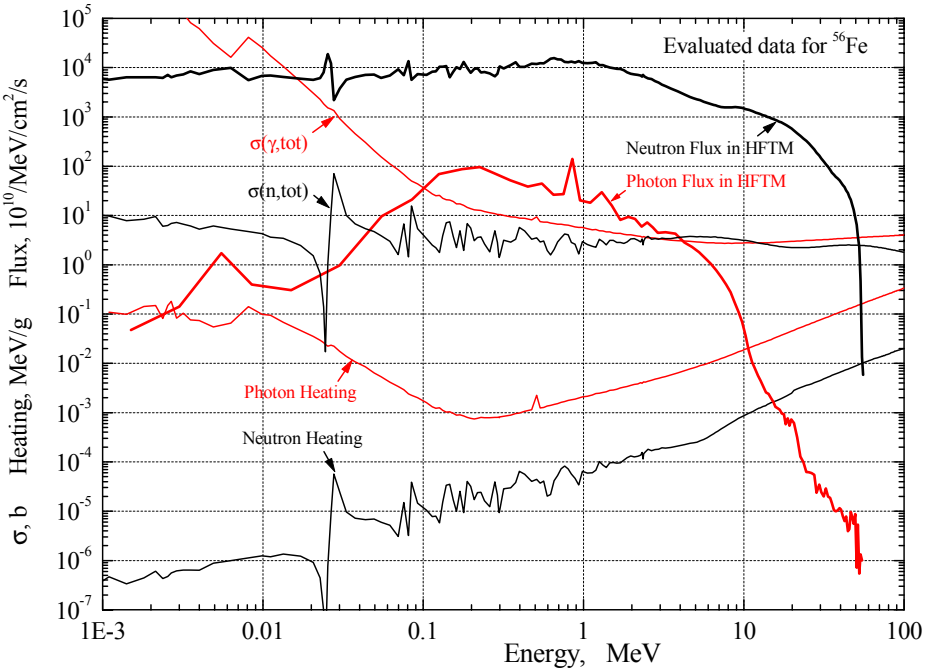

Fig. 17. Neutron (black curve) and photon (red) reaction cross sections and heating for ^{56}Fe, data from LANL -150. Thick lines show the IFMIF neutron and photon spectral fluxes averaged over the HFTM volume.

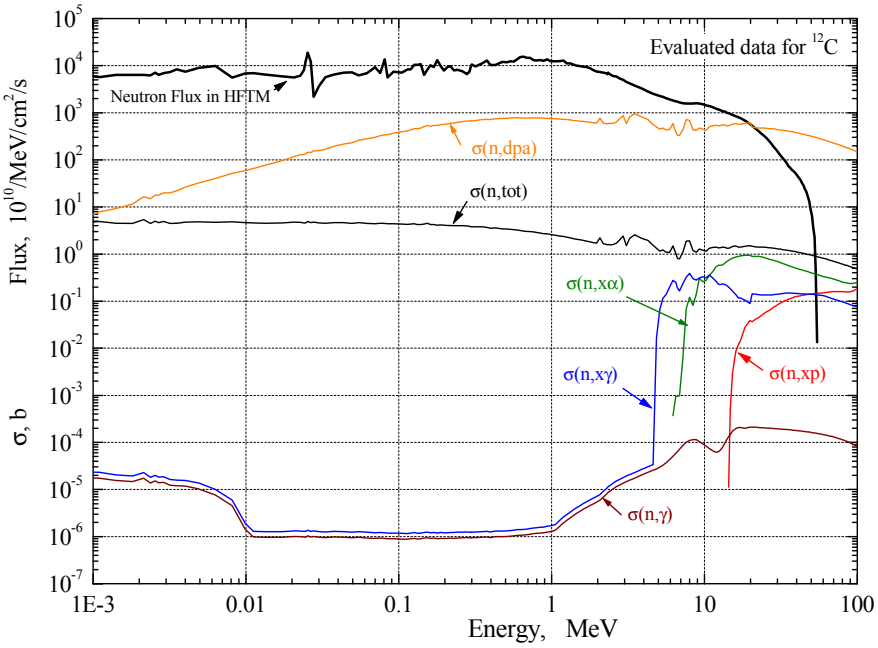

Fig. 18. Neutron reaction cross sections for ^{12}C as evaluated by LANL (thin solid lines). Thick line shows the IFMIF neutron spectal flux averaged over the HFTM.

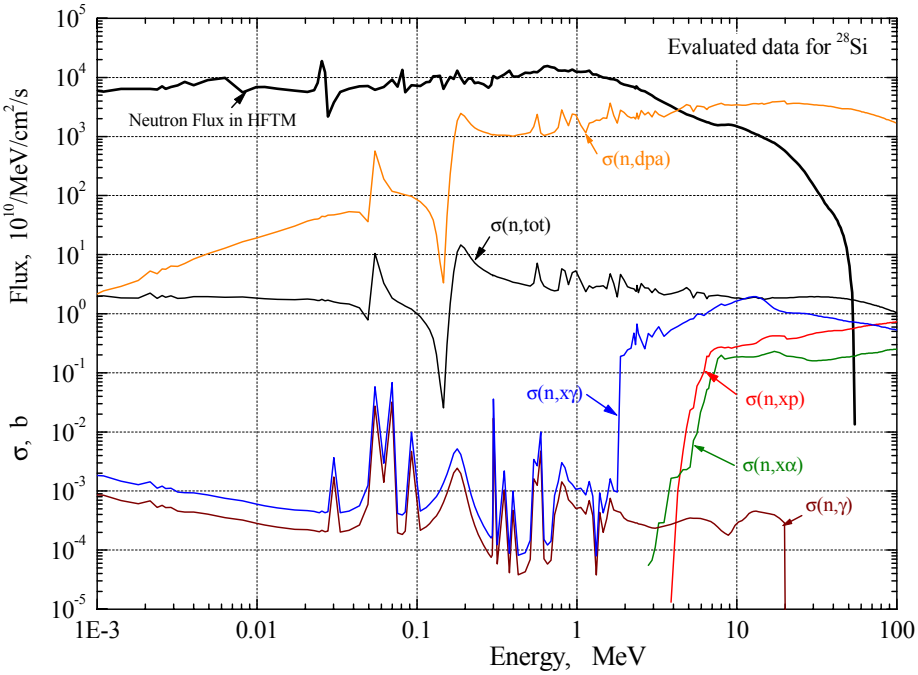

Fig. 19. Neutron reaction cross sections for ^{28}Si as evaluated by LANL (thin solid lines). Thick line shows the IFMIF neutron spectal flux averaged over the HFTM.

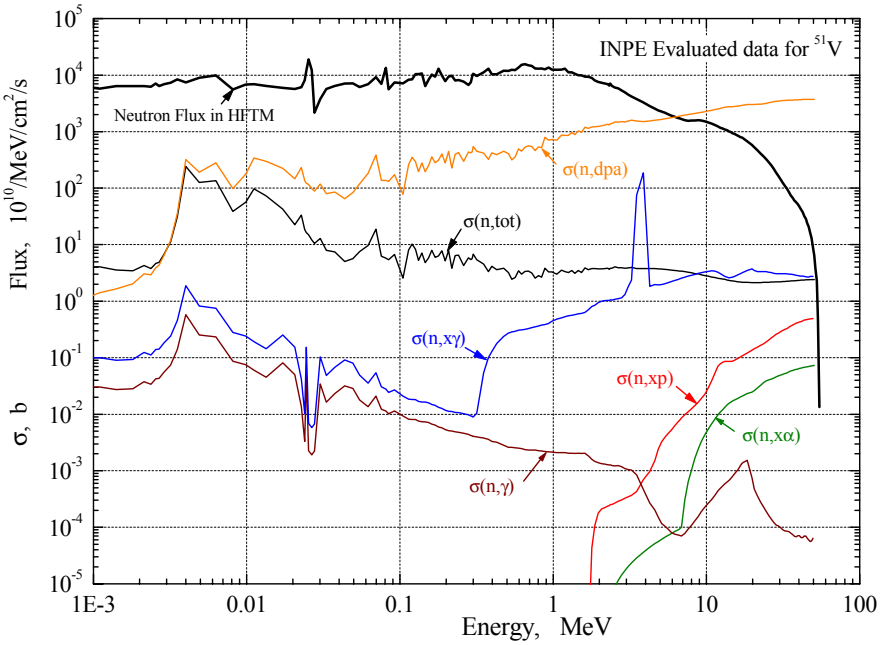

Fig. 20. Neutron reaction cross sections for ^{51}V as evaluated by INPE (thin solid lines). Thick line shows the IFMIF neutron spectal flux averaged over the HFTM.

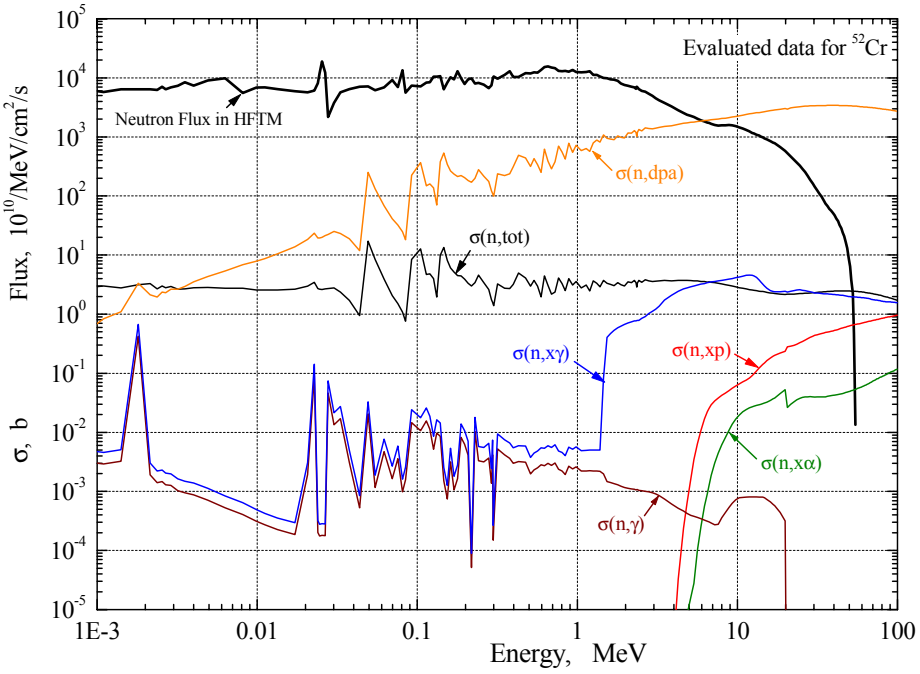

Fig. 21. Neutron reaction cross sections for ^{52}Cr as evaluated by LANL (thin solid lines). Thick line shows the IFMIF neutron spectal flux averaged over the HFTM.

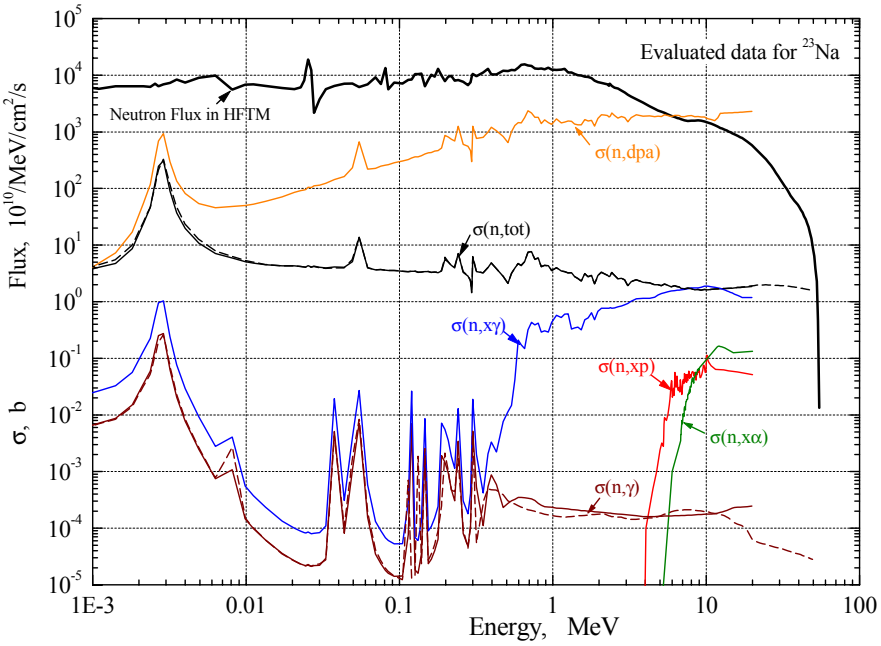

Fig. 22. Neutron reaction cross sections for ^{23}Na as evaluated by ENDF/B-VI (thin solid lines) and INPE (dashed lines). Thick line shows the IFMIF neutron spectal flux averaged over the HFTM.

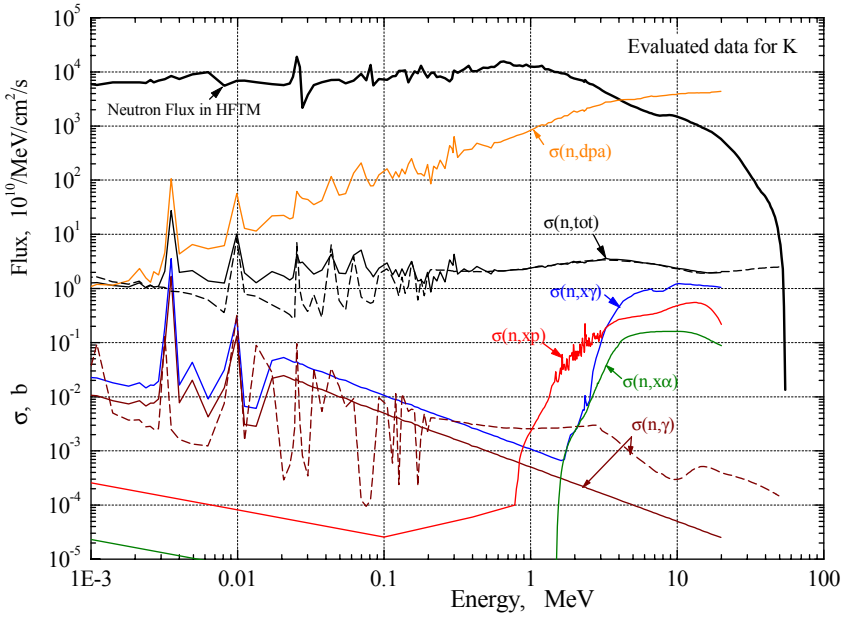

Fig. 23. Neutron reaction cross sections for K as evaluated by ENDF/B-VI (^{nat}K, thin solid lines) and INPE (^{39}K, dashed lines). Thick line shows the IFMIF neutron spectal flux averaged over the HFTM.

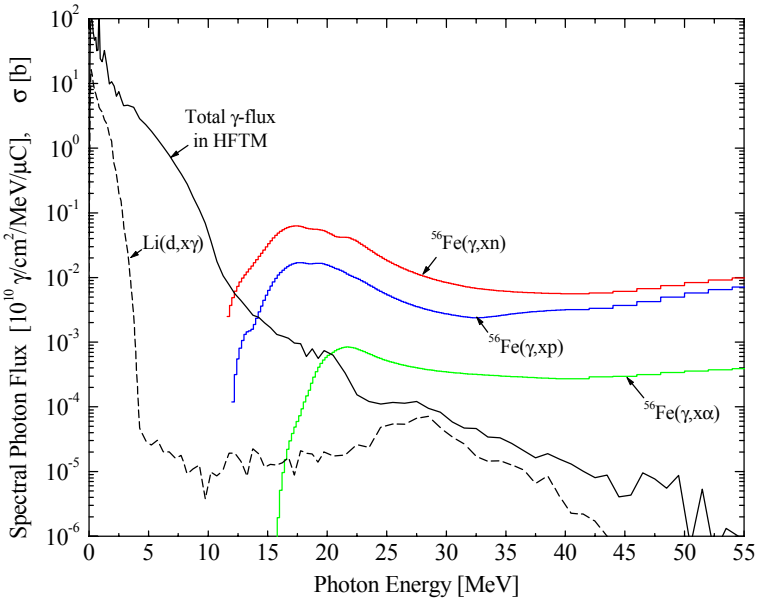

Fig. 24. Photon induced nuclear reactions cross sections on ^{56}Fe and γ-rays spectral flux averaged over the HFTM volume (dashed curve - from the Li(d,xγ) source, solid – from the source and produced in Eurofer).

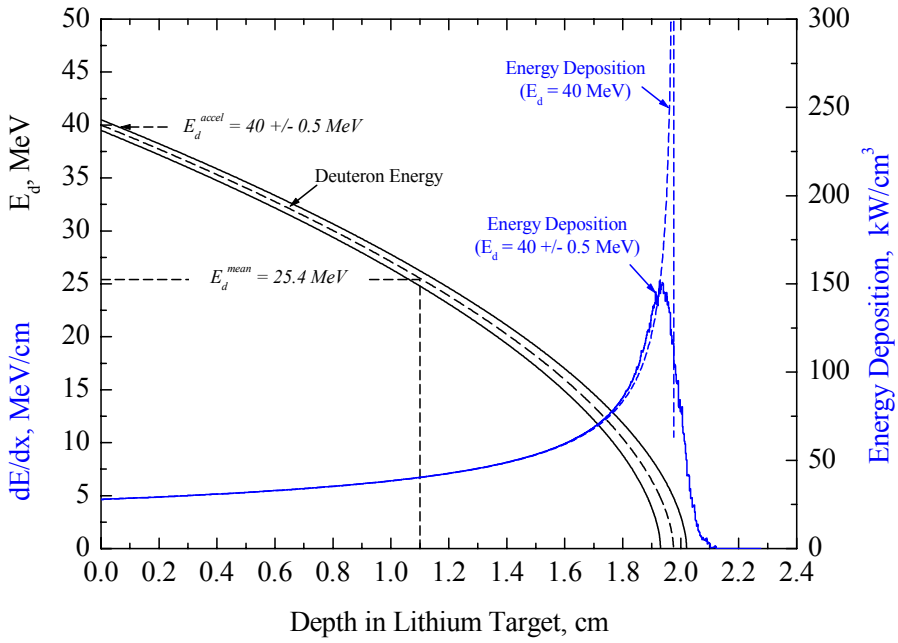

Fig. 25. Deuteron energy (black curves) and total energy deposition (blue curves) in the Li target versus the track length. Dashed curve – monoenergetic 40 MeV beam, solid – Gaussian energy distribution with root mean square 0.5 MeV.

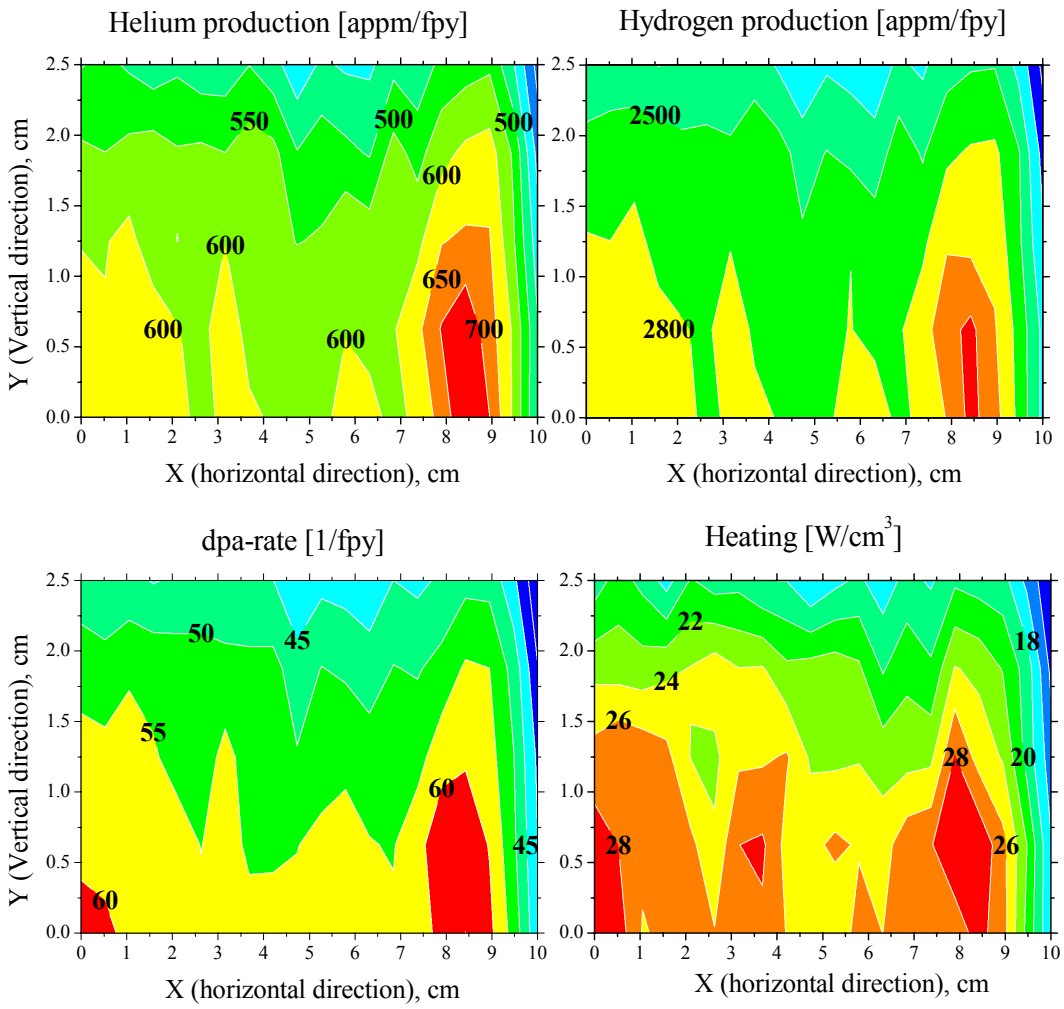

Fig. 26. Spatial distribution of the gas production, dpa-rate and heat released in a quarter of the lithium target back plate (20×5×0.18 cm, EUROFER, normal density) during IFMIF full performance (250 mA × 40 MeV deuteron beam).

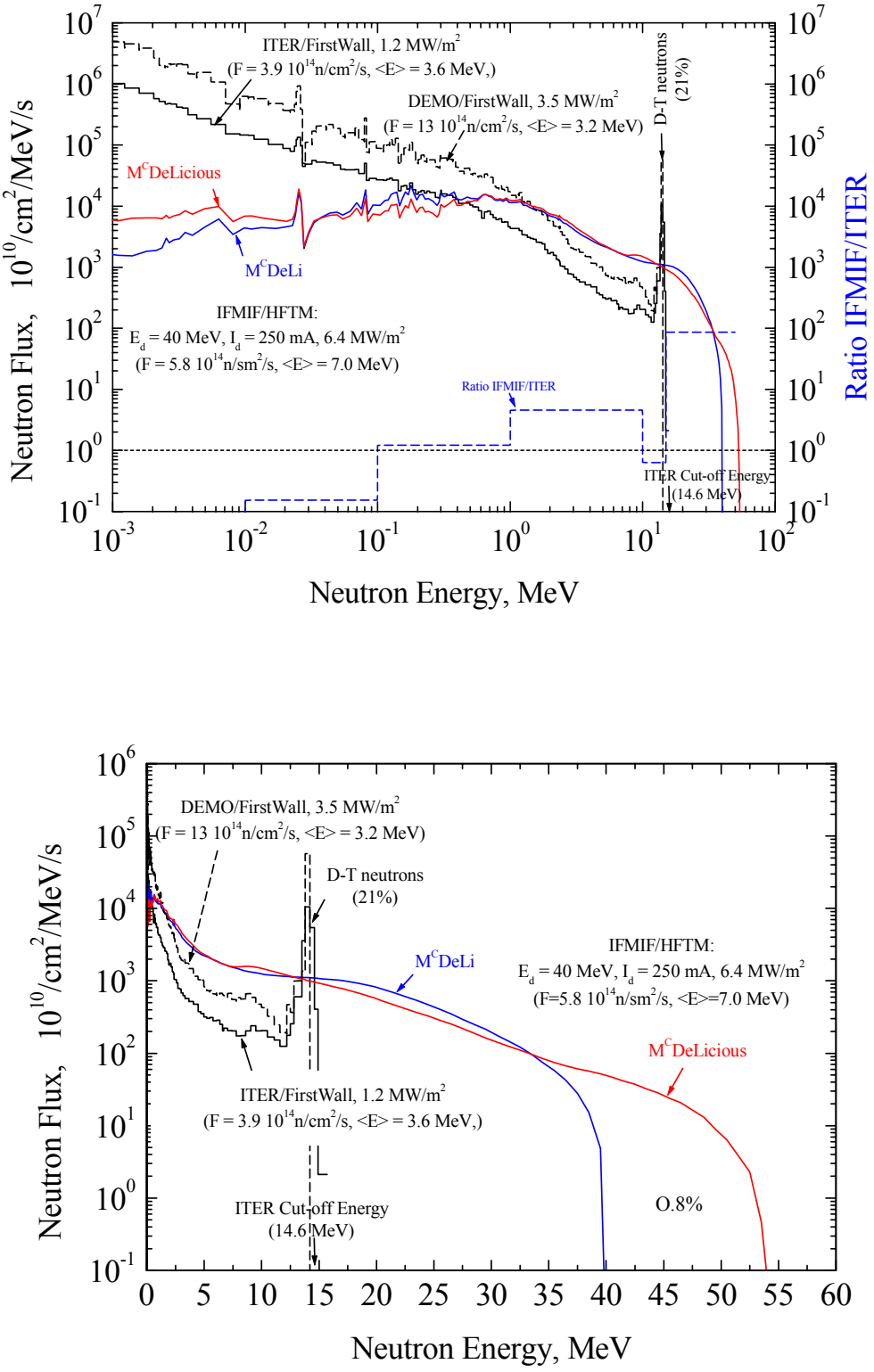

Fig. 27. Neutron flux spectral distributions in the HFTM as calculated by the M^{C}DeLicious (red curve) and M^{C}DeLi (blue) codes are shown in the logarithmic (upper part) and linear (bottom) energy scale. For comparison the ITER (solid histogram) and DEMO (dashed) first wall neutron spectra are depicted.

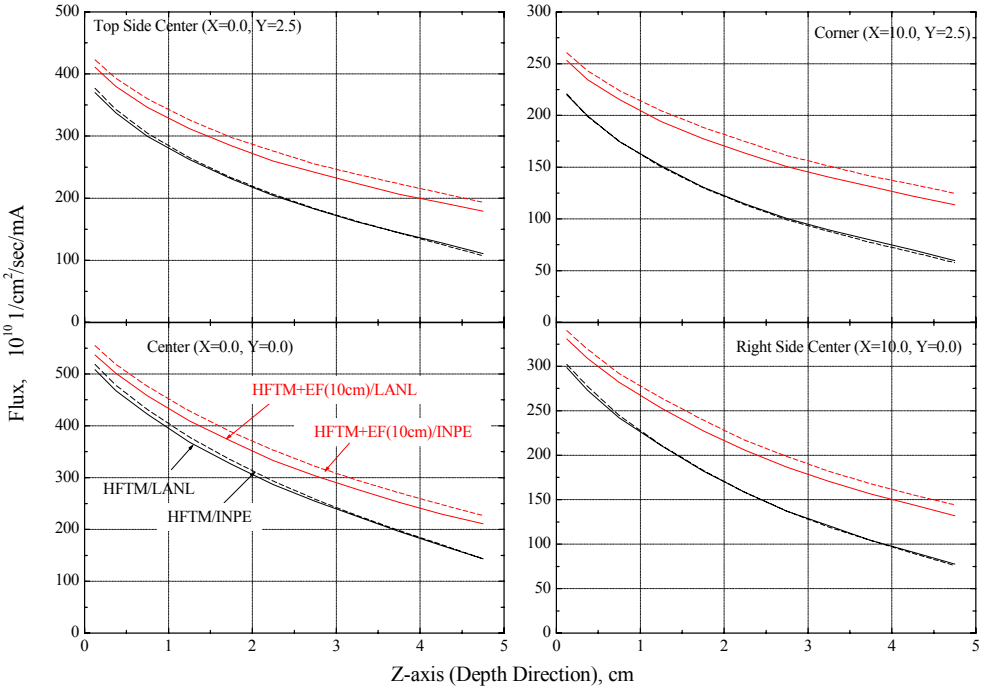

Fig. 28. Spatial distribution of the neutron flux in the HFTM, calculated with LANL and INPE libraries without and with reflector (EUROFER of 10 cm thickness).

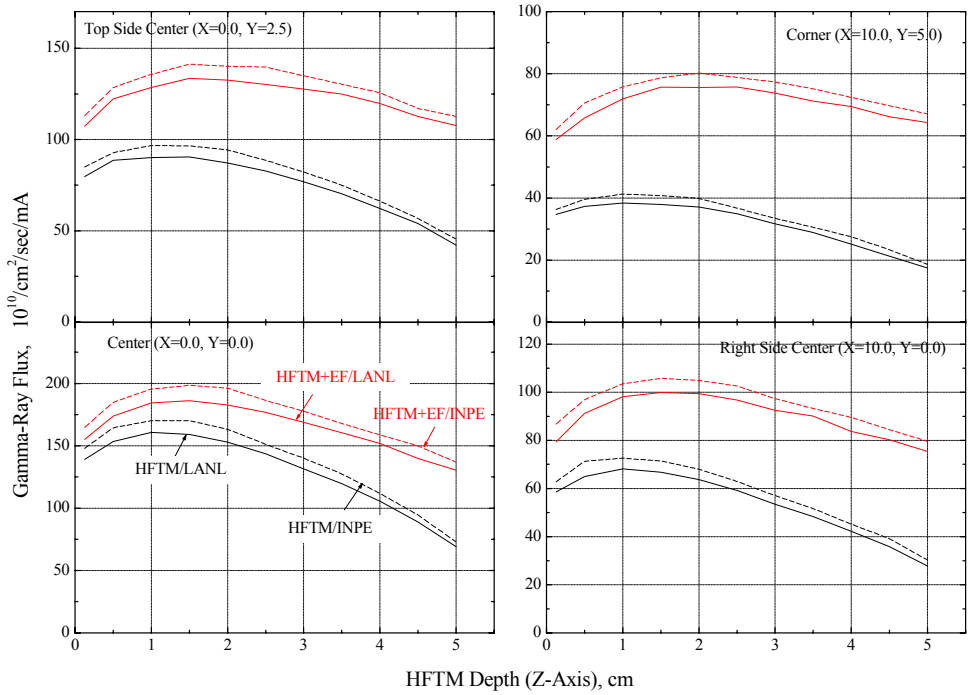

Fig. 29. Spatial distribution of the γ-ray fluxe in the HFTM, calculated with LANL and INPE libraries without and with reflector (EUROFER of 10 cm thickness).

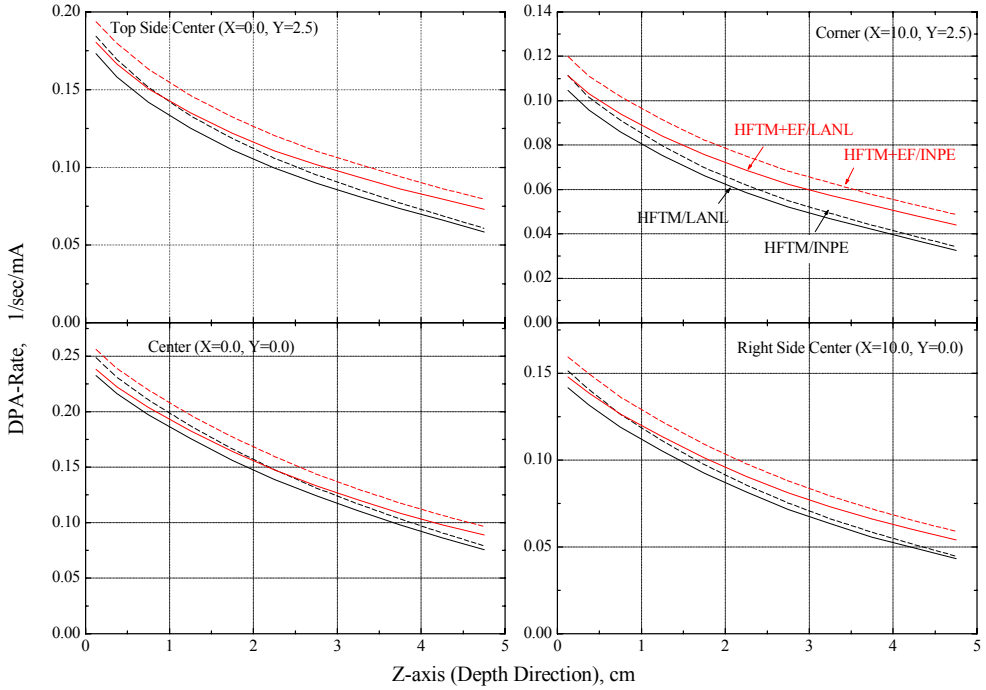

Fig. 30. Spatial distribution of the dpa-rates in the HFTM, calculated with LANL and INPE libraries without and with reflector (EUROFER of 10 cm thickness).

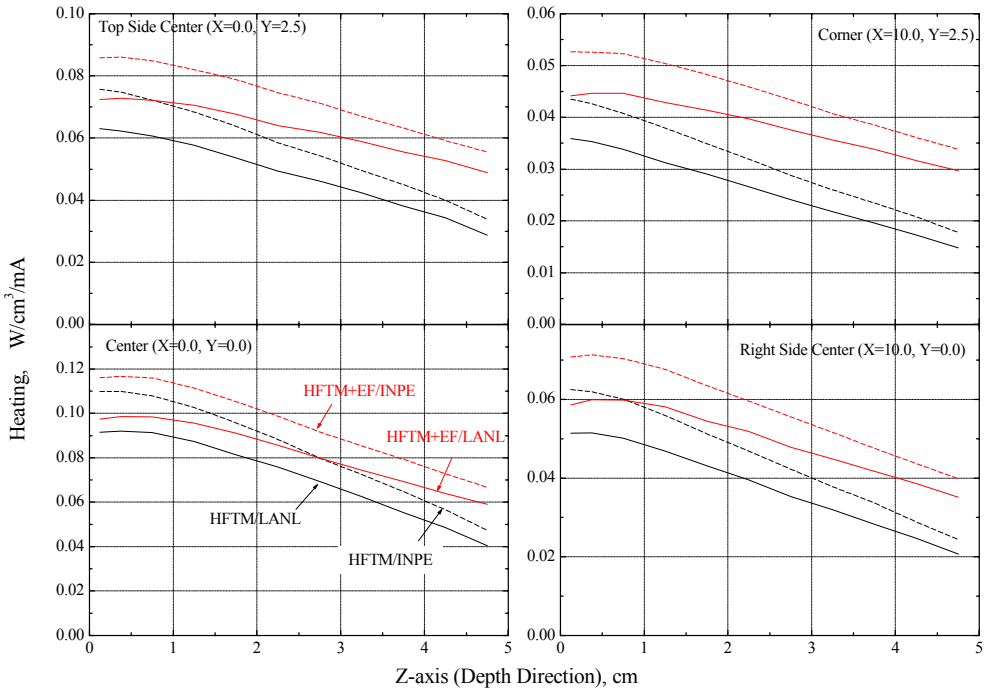

Fig. 31. Spatial distribution of the heat released in the HFTM, calculated with LANL and INPE libraries without and with reflector (EUROFER of 10 cm thickness).

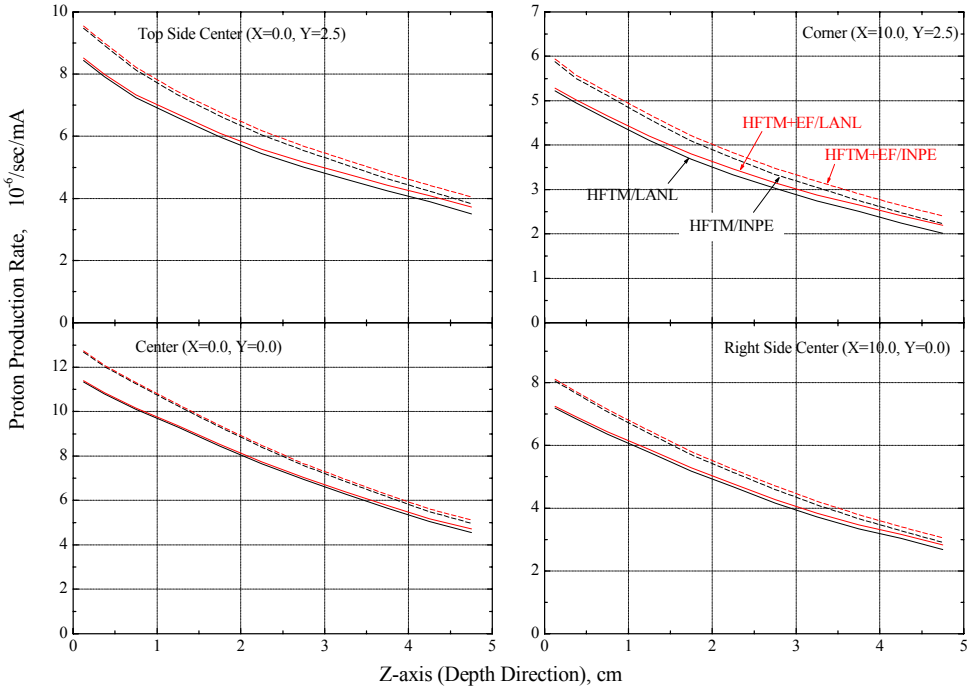

Fig. 32. Spatial distribution of the hydrogen production in the HFTM, calculated with LANL and INPE libraries without and with reflector (EUROFER of 10 cm thickness).

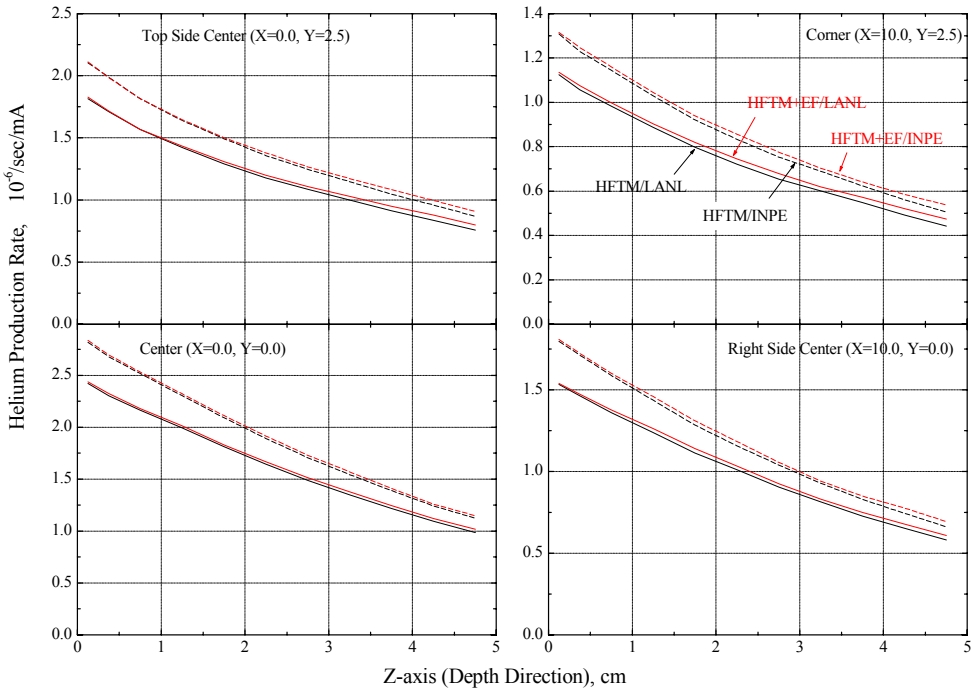

Fig. 33. Spatial distribution of the helium production rate in the HFTM, calculated with LANL and INPE libraries without and with reflector (EUROFER of 10 cm thickness).

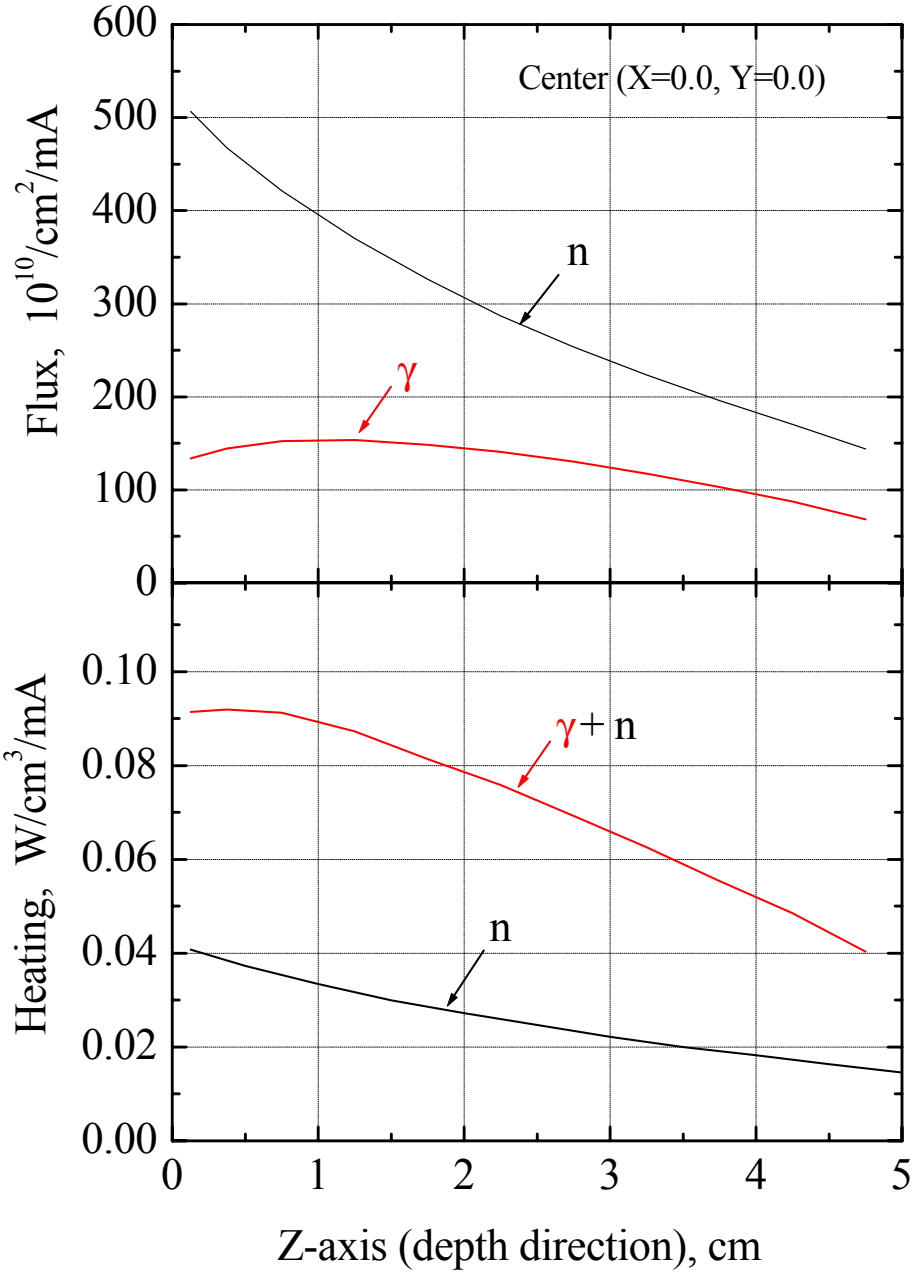

Fig. 34. Dependence of the neutron and γ-ray fluxes (top) and heat production rate (bottom) on the depth in HFTM along symmetry axis, calculated with LANL libraries.

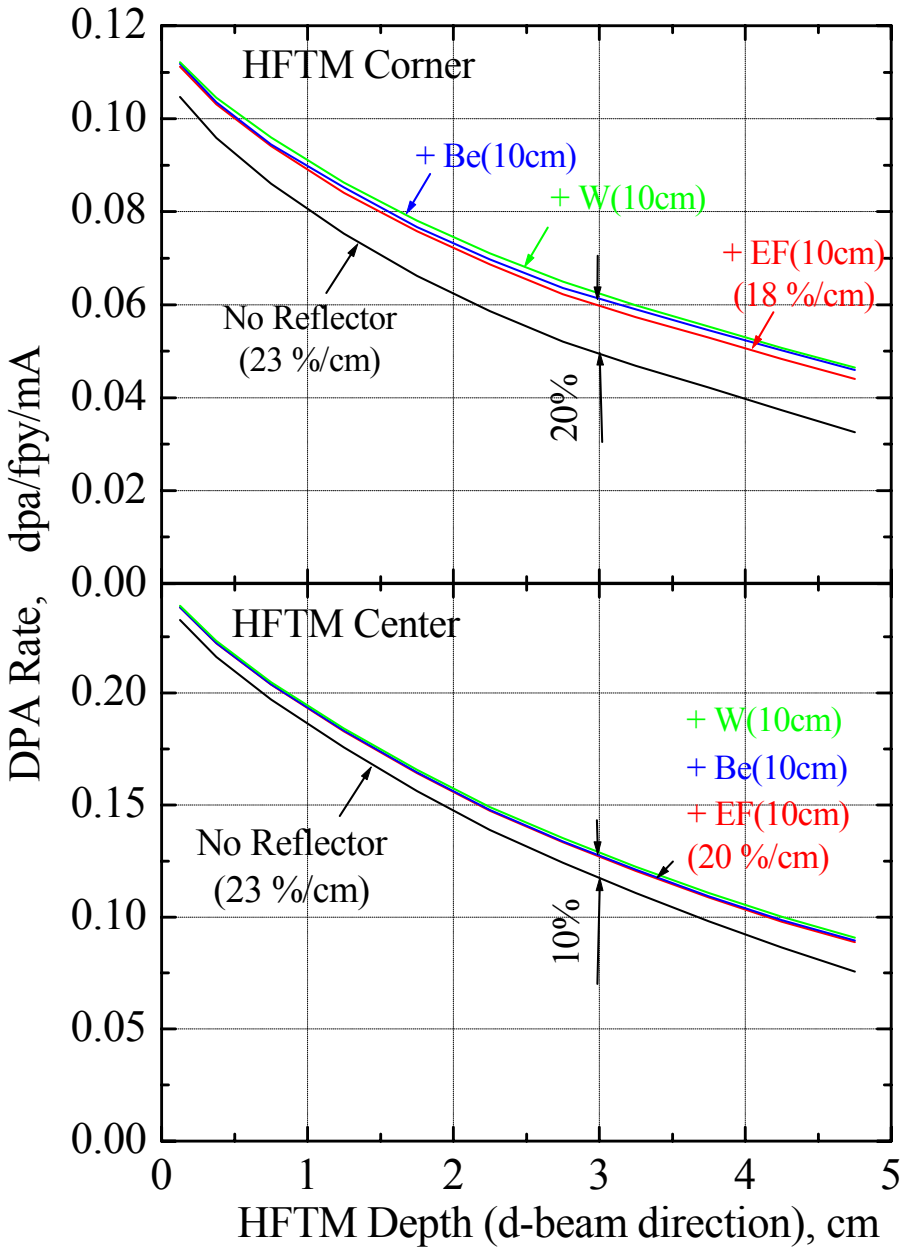

Fig. 35. Dpa rate as a function of the depth in HFTM along its corner (top) and symmetry axis (bottom). Black curve – bare test module; red, blue and green curves – module surrounded by Eurofer (EF), Beryllium and Tungsten reflectors.

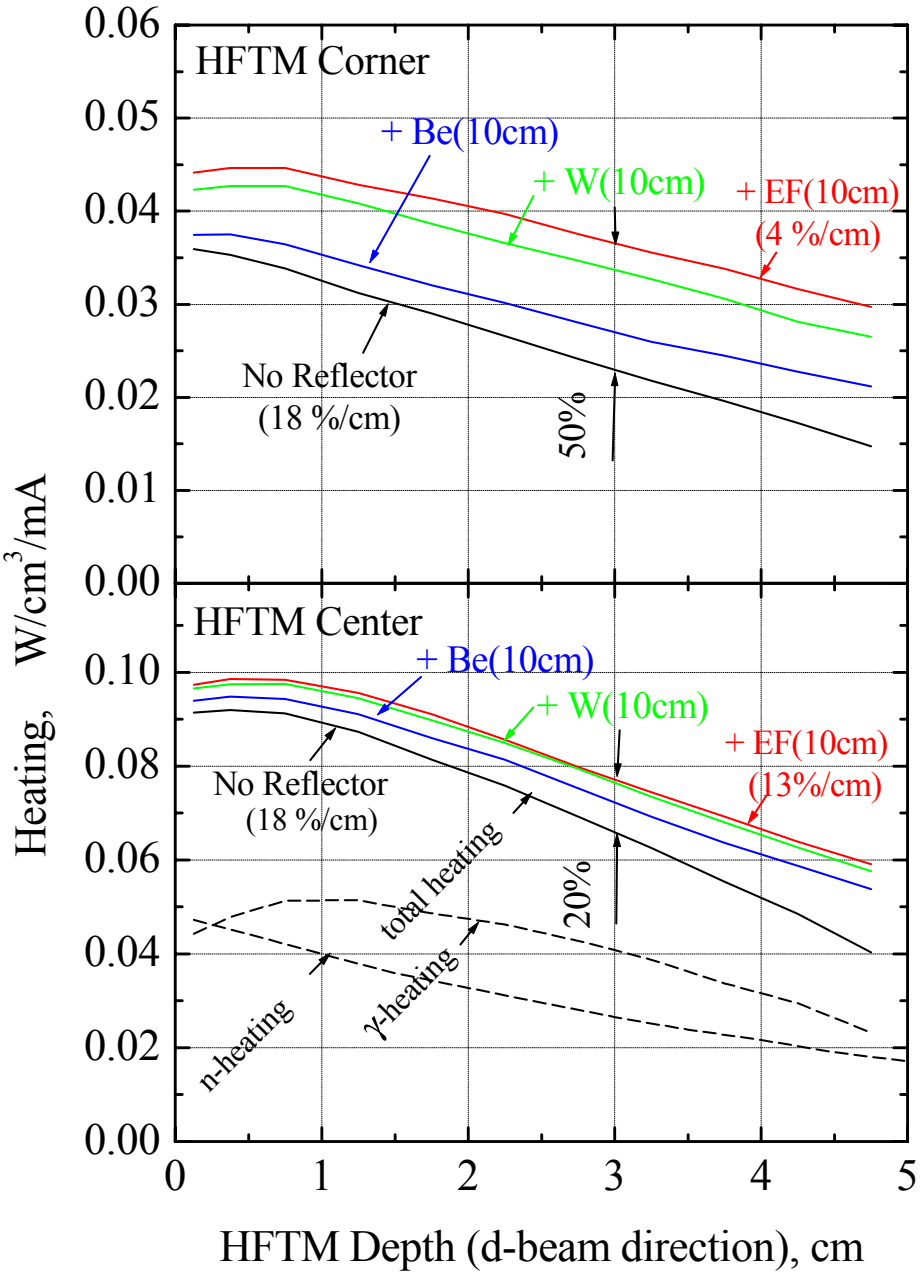

Fig. 36. Heat production as a function of the depth in HFTM along its corner (top) and symmetry axis (bottom). Black solid curve – bare test module; red, blue and green curves – module surrounded by Eurofer (EF), Beryllium and Tungsten reflectors. Dashed curves show the heating due to neutrons and photons.

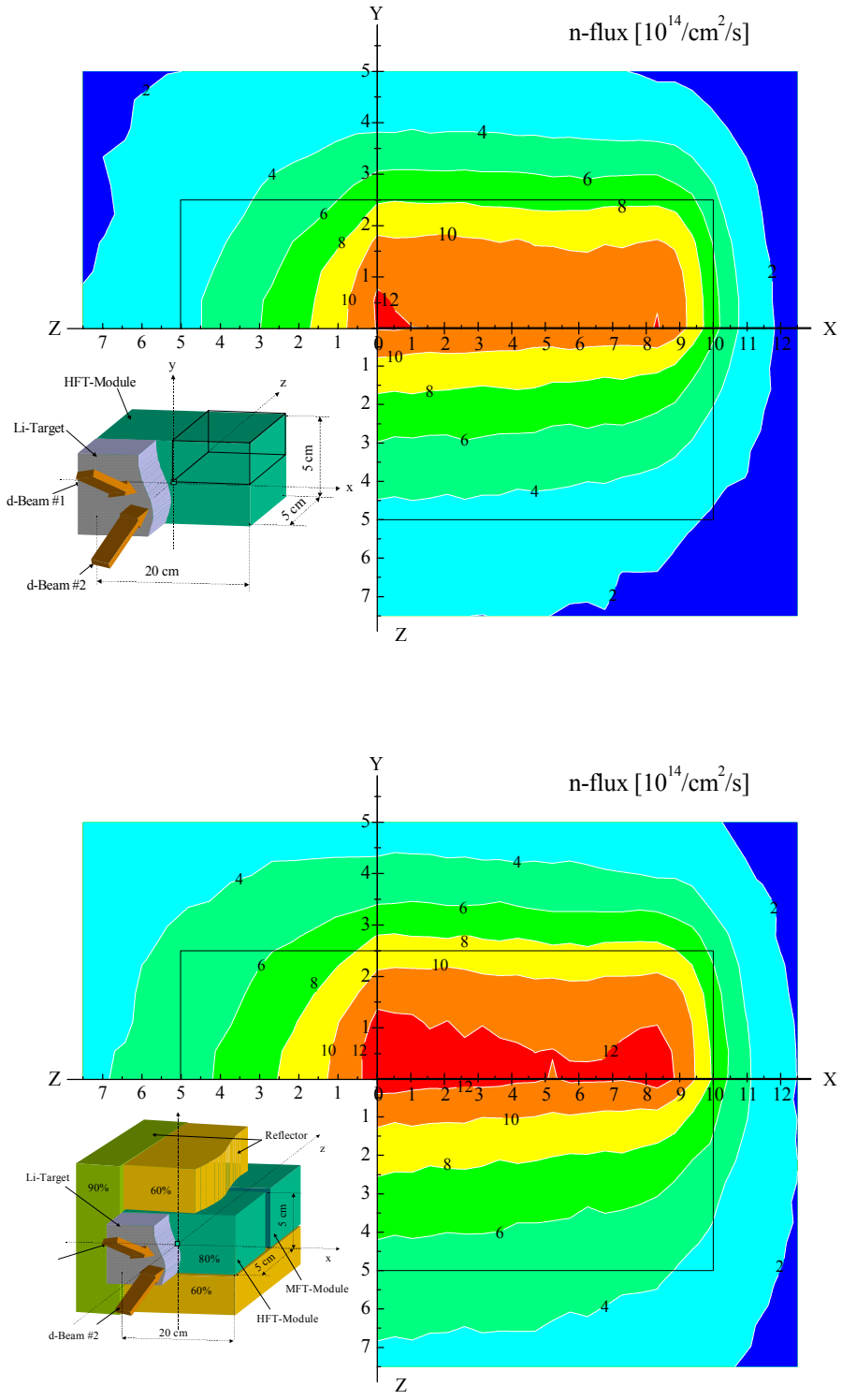

Fig. 37. Neutron flux in and around the HFTM without (top) and with EUROFER reflector of 10 cm thickness (bottom). Black lines show geometrical boundaries of the test module ($20\times5\times5$ cm^3).

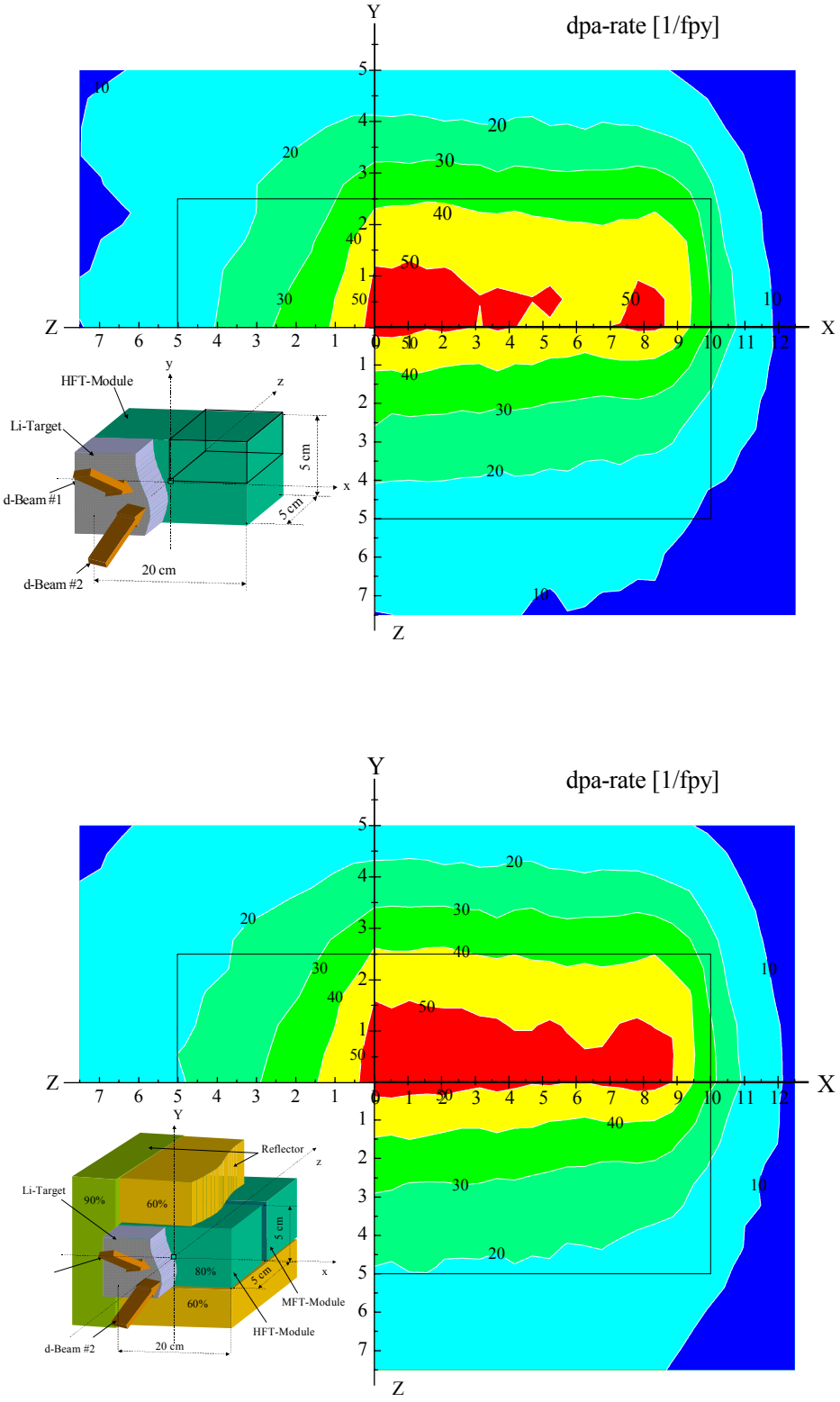

Fig. 38. dpa-rates in and around the HFTM without (top) and with EUROFER reflector of 10 cm thickness (bottom). Black lines show geometrical boundaries of the test module ($20\times5\times5$ cm^3).

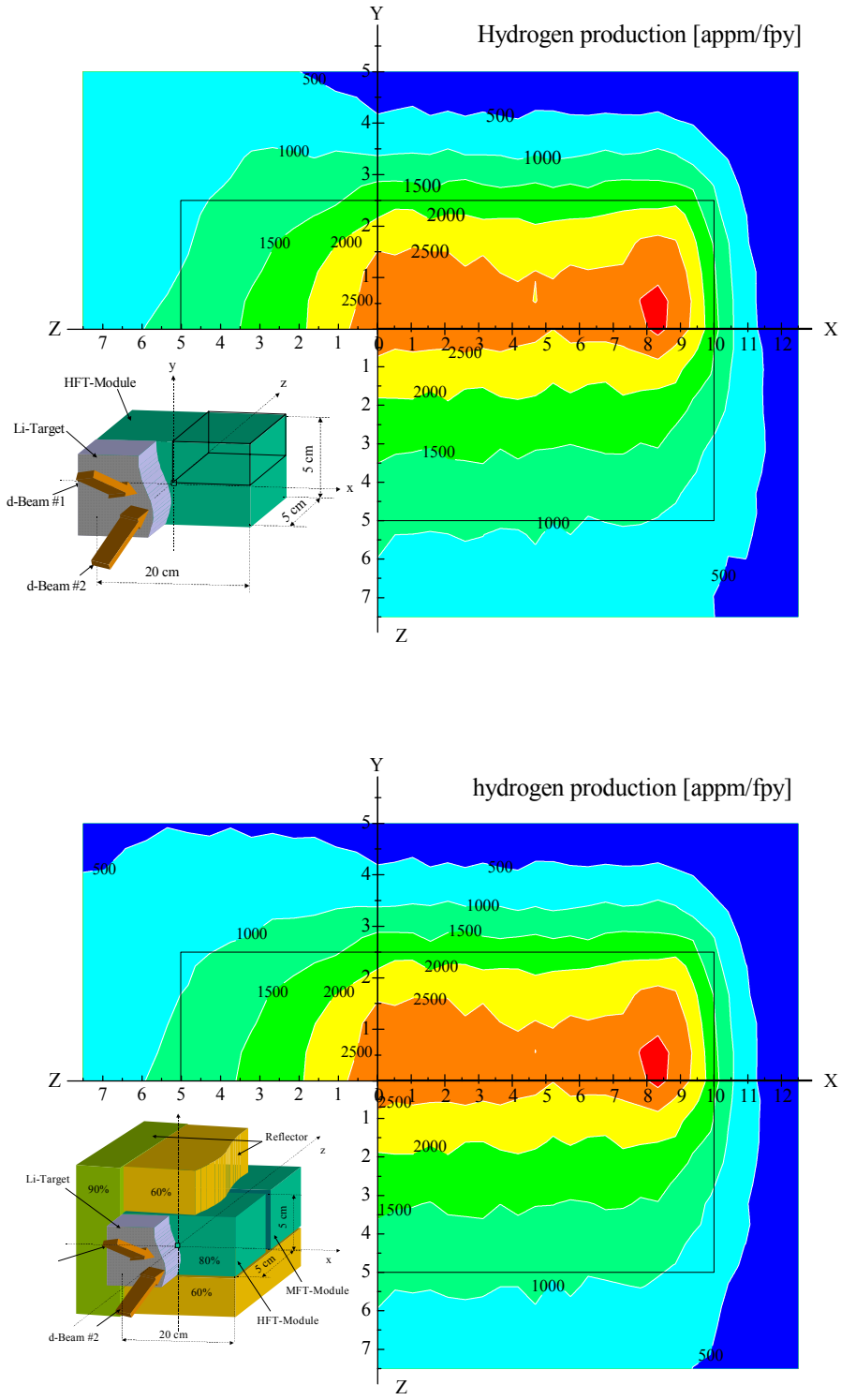

Fig. 39. Hydrogen production in and around the HFTM without (top) and with EUROFER reflector of 10 cm thickness (bottom). Black lines show geometrical boundaries of the test module (20×5×5 cm^3).

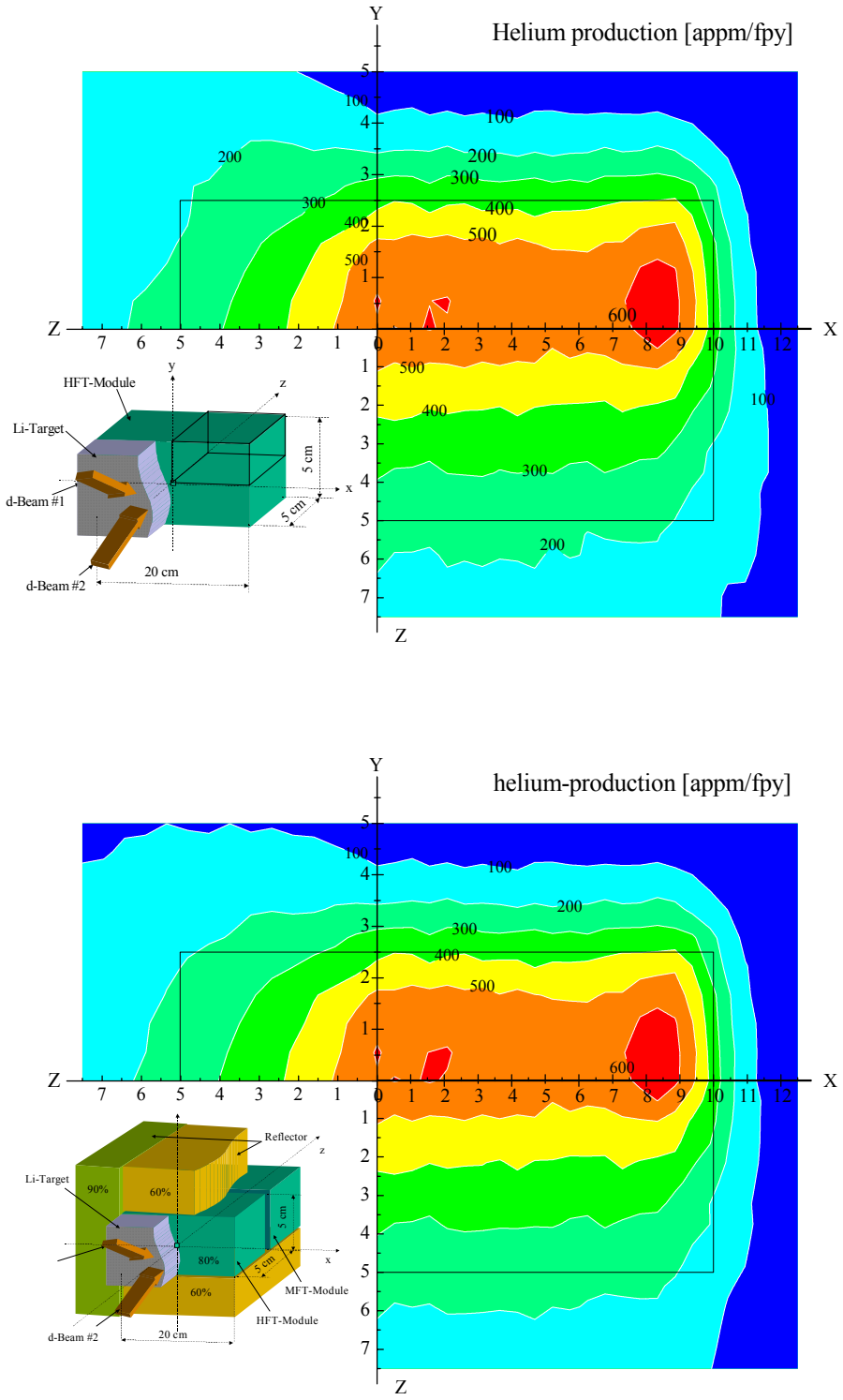

Fig. 40. Helium production in and around the HFTM without (top) and with EUROFER reflector of 10 cm thickness (bottom). Black lines show geometrical boundaries of the test module (20×5×5 cm^3).

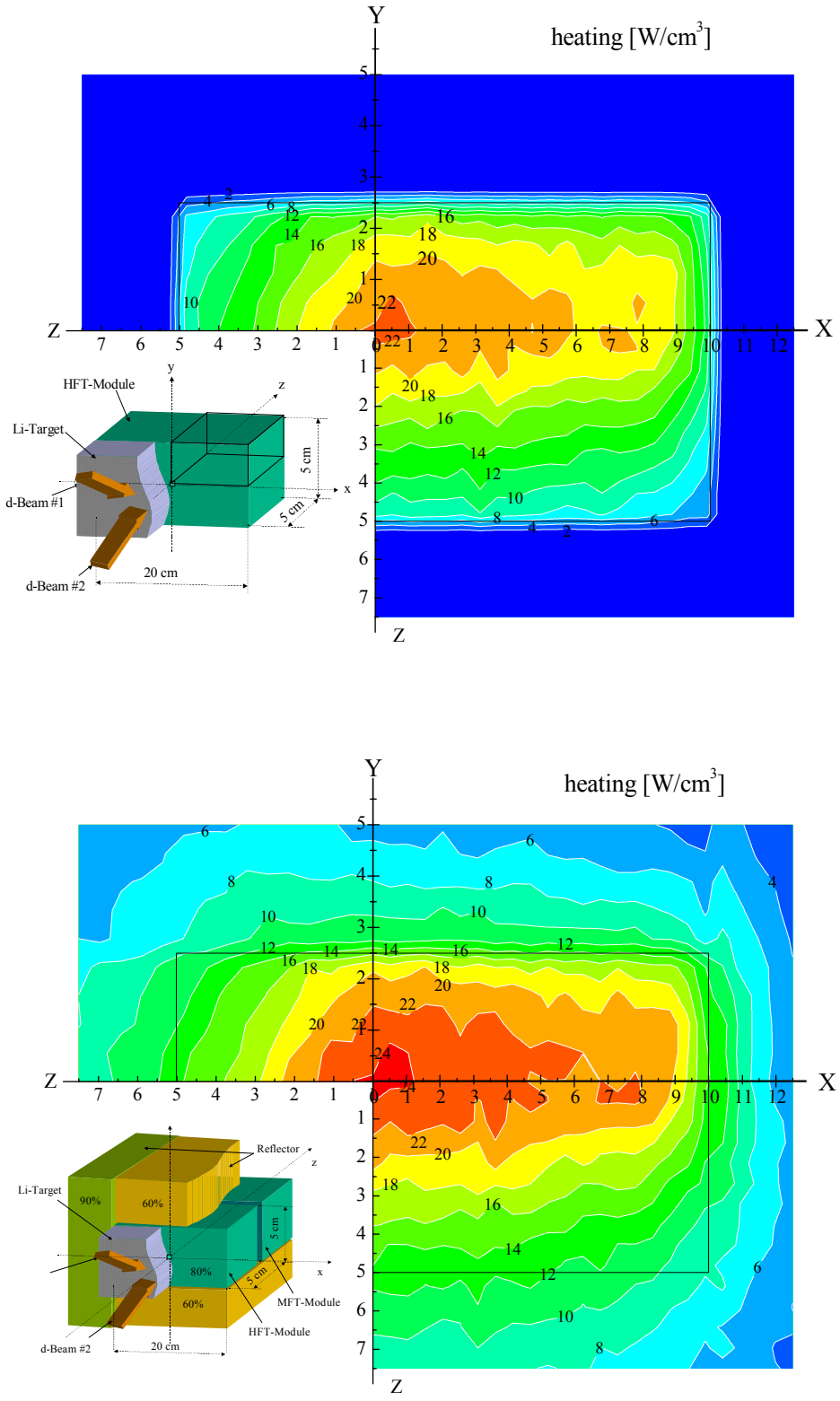

Fig. 41. Heat production in and around the HFTM without (top) and with EUROFER reflector of 10 cm thickness (bottom). Black lines show geometrical boundaries of the reference test module (20×5×5 cm^3).

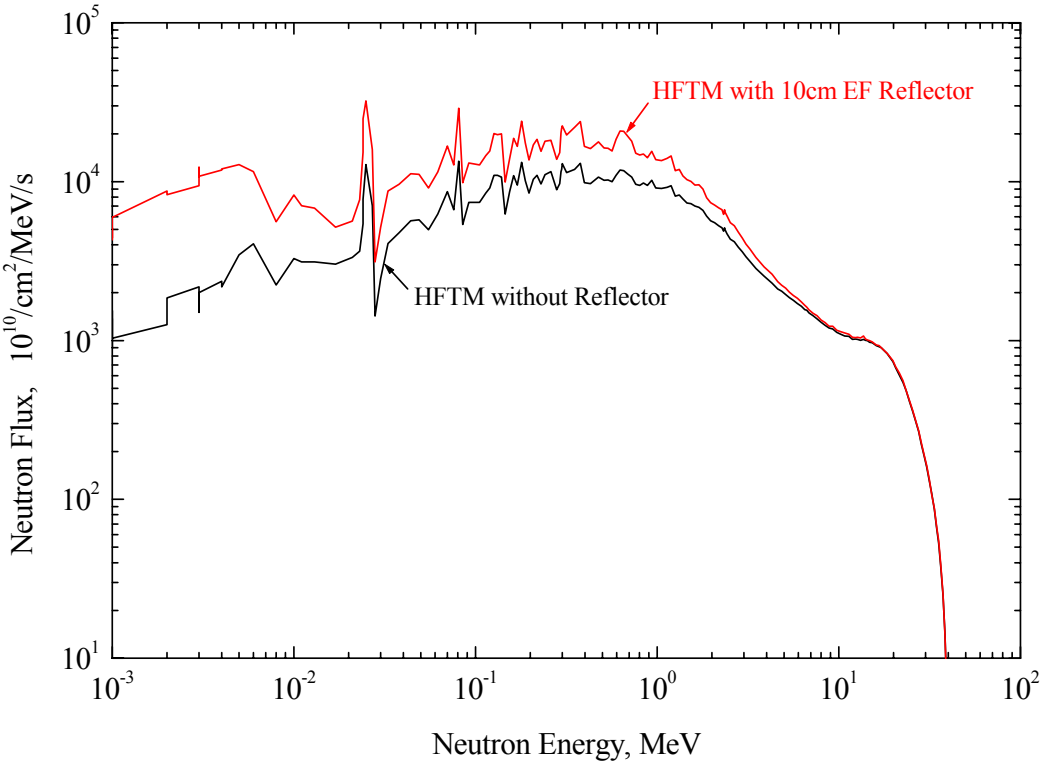

Fig. 42. Spectral neutron flux averaged over bare HFTM (black curve) and surrounded by EUROFER reflector of 10 cm thickness (red curve).

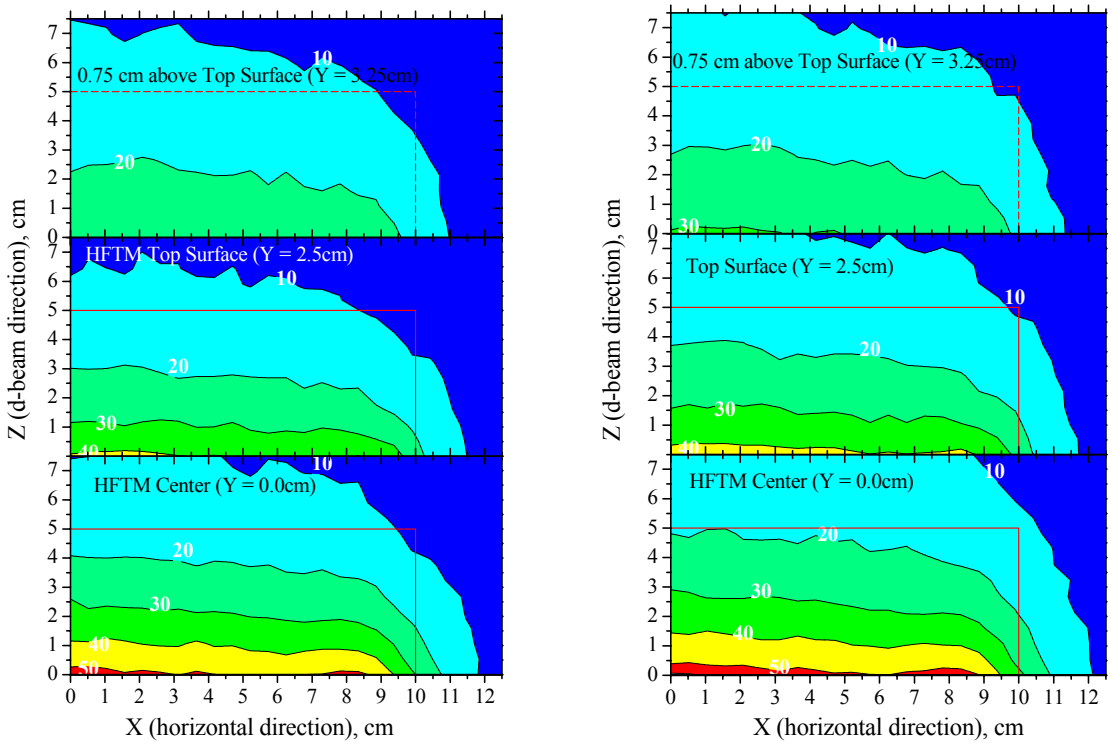

Fig. 43. Countour plot for the damage production (dpa/fpy) in the bare test module (left) and surrounded by 10cm Eurofer reflector (right) at 3 vertical levels: center and top surfaces of HFTM and 0.75 cm above it. Red lines show geometrical boundaries of the test module (20×5×5 cm^3).

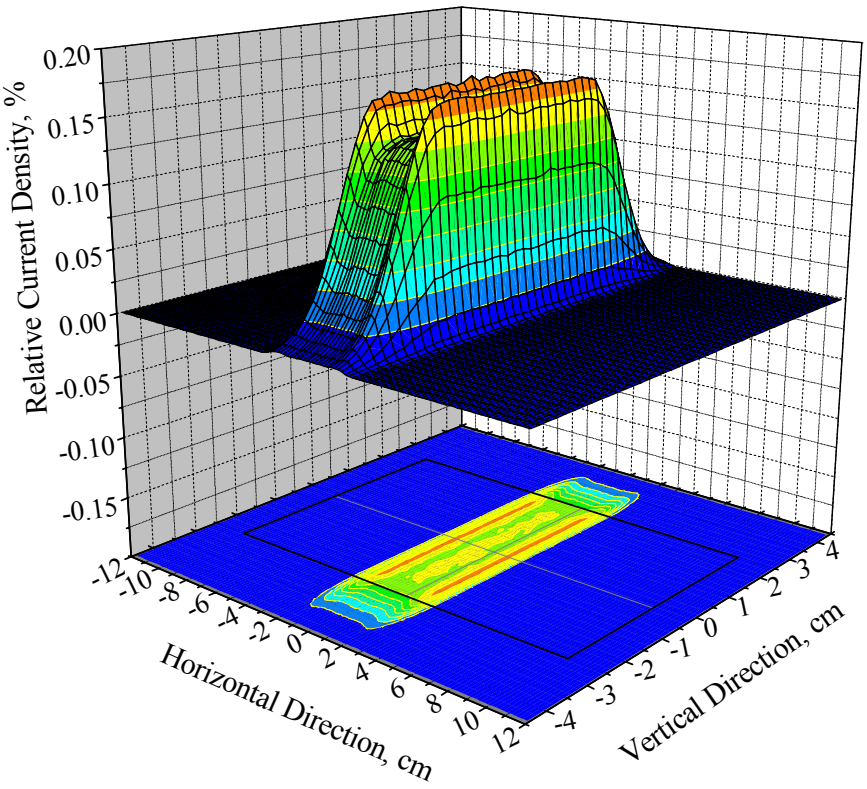

Fig. 44. Three-dimensional (top) and contour plot (bottom) presentation of the IFMIF deuteron beam profile for the reduced beam foot print 4×5 cm^2. The box on the projection plane shows the front plate contour (20×5 cm^2) of the reference HFTM.

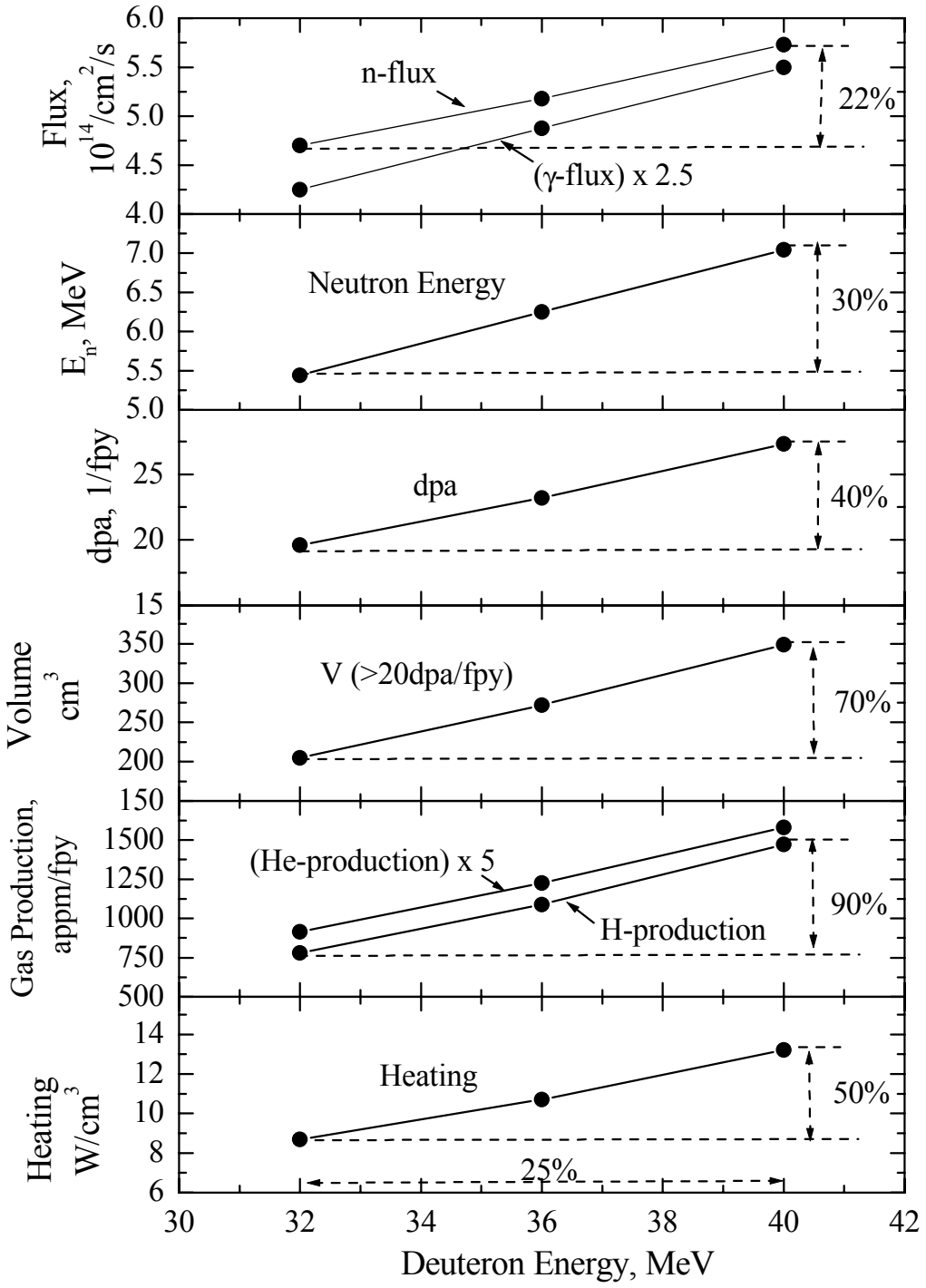

Fig. 45 Dependence of main neutronics parameters averaged over HFTM volume on incident deuteron energy, given total beam current is 250 mA.